Environmental Science

AIMS Environmental Science, 12(4): 653–682.
DOI: 10.3934/environsci.2025029
Received: 04 October 2024
Revised: 20 June 2025
Accepted: 25 June 2025
Published: 10 July 2025

http://www.aimspress.com/journal/environmental

Research article

Removal of lead (II) from aqueous solutions using iron nanoparticles synthesized from watermelon peel extract

Hugo Sánchez-Moreno[1], Kevin Altamirano[2], Sandra Escobar[3], Nelly Guananga-Díaz[3], Verónica Cando[4], Luis Anilema[2] and Israel Heredia[2]

[1] Alternative Energies and Environment Research Group, Faculty of Sciences, Escuela Superior Politécnica de Chimborazo (ESPOCH), Panamericana Sur Km 1 ½, Chimborazo, EC060155, Ecuador
[2] Independent researcher
[3] Leishmaniasis and other parasitic diseases in Ecuador research group, Faculty of Sciences, Escuela Superior Politécnica de Chimborazo (ESPOCH), Panamericana Sur Km 1 ½, Chimborazo, EC060155, Ecuador
[4] Biomedical research, technology and pharmaceutical care group of Ecuador, Faculty of Sciences, Escuela Superior Politécnica de Chimborazo (ESPOCH), Panamericana Sur Km 1 ½, Chimborazo, EC060155, Ecuador

* **Correspondence:** Email: hugoj.sanchez@espoch.edu.ec; Tel: 0987983888.

Abstract: In this research, we explored the synthesis and application of iron oxide magnetic nanoparticles functionalized with watermelon peel extract (NP-FeO-CL) using an eco-friendly approach. These nanoparticles were characterized by FT-IR, SEM, and UV-Visible spectroscopy, confirming their structure, magnetic properties, and purity. Their efficiency was evaluated in removing lead (Pb) ions from aqueous solutions under various experimental conditions, including variations in contact time, adsorbent mass, pH, temperature, and initial Pb concentration. The results showed a maximum Pb removal of 91.40% under optimum conditions (pH = 4, temperature = 25 °C, and contact time = 5 min). Adsorption isotherms indicated an excellent fit to the Freundlich model (R^2 = 0.94, KF = 16.99 mg/g, n = 1.97), reflecting heterogeneous and multi-layered adsorption. Likewise, a good fit to the Langmuir model (R^2 = 0.91) was observed, suggesting a single-layer adsorption with a maximum adsorption capacity q_{max} of 47.16 mg/g. As for the kinetics, the pseudo-second order model adequately

described the process ($R^2 = 0.99$), suggesting that the adsorption rate is controlled by the availability of active sites. Thermodynamic analysis evidenced that the process is spontaneous and favorable at moderate temperatures, although the efficiency decreases at higher temperatures. This study highlights the potential of NP-FeO-CL as a sustainable and efficient solution for the remediation of water contaminated with heavy metals. Moreover, the green synthesis method used not only minimizes the environmental impact but also promotes the reuse of agro-industrial waste, contributing to the circular economy. Tests conducted under real conditions, such as in mining waters fortified with Pb, validated its practical applicability, achieving efficiencies above 90% in the first minutes of the process. These results position NP-FeO-CL as a versatile tool for treating contaminated water, with a significant impact on the sustainable management of water resources and environmental protection.

Keywords: Pb adsorption; mining wastewater treatment; green synthesis; adsorption isotherms; nanoparticles

Highlights:

- The characteristics of the adsorbent were studied using SEM, EDS, and FTIR.
- The adsorption process was influenced by key operating parameters, including equilibrium time, adsorbent dosage, pH, temperature, and initial Pb (II) concentration.
- Nanoparticles synthesized from watermelon peel extract (NP-FeO-CL) are effective and sustainable adsorbents for Pb (II).
- The Langmuir model provided the best fit, with a maximum adsorption capacity of 47.16 mg/g.
- The pseudo second-order kinetic model best describes the adsorption mechanism.
- Effective adsorption of Pb (II) in real mine water was achieved, reaching 91.40%.

1. Introduction

Contamination by heavy metals, such as lead (Pb), represents a global threat due to its toxicity, bioaccumulation, and persistence in the environment[1]. This non-essential metal for living organisms can seriously affect human health, damaging vital systems such as the nervous, renal, and skeletal systems, especially in vulnerable populations such as children and pregnant women. Prolonged exposure to lead also has a negative impact on aquatic and terrestrial ecosystems [2]. In Ecuador, several regions present alarming concentrations of lead in water sources due to industrial and agrochemical activities, which underlines the urgency of developing sustainable and accessible solutions for its remediation. In Ecuador, the presence of lead in groundwater has emerged as a critical concern, affecting several regions of the country and presenting a serious risk to public health [3]. Prolonged exposure to lead can have devastating effects on human health, affecting various body systems, including the skin, brain, liver, kidneys, and bones. Children, in particular, are more vulnerable to the neurotoxic effects of lead, making it urgent to find effective and sustainable solutions for the remediation of this contamination [4].

Traditional approaches to heavy metal removal, such as ion exchange, chemical precipitation, and membrane processes, although effective, have significant disadvantages [5]. These methods are often costly, energy-intensive, and generate chemical by-products that pose new environmental challenges [5]. In the face of these limitations, adsorbent materials have emerged as promising alternatives due to their efficiency, low cost, and ability to minimize secondary impacts. Among the most studied materials are activated carbons, zeolites, biopolymers, and, more recently, metal oxide nanoparticles [6].

Iron oxide nanoparticles functionalized with watermelon peel extract (NP-FeO-CL) stand out in this field due to their high adsorption capacity, magnetic properties, and the possibility of being easily recycled by magnetic separation [7]. These properties, combined with their high surface area and the presence of reactive functional groups, make them ideal candidates for metal ion removal. In addition, the synthesis of NP-FeO-CL using green methods has gained great interest, as it reduces the dependence on toxic reagents and takes advantage of agro-industrial wastes as sources of precursor chemicals. In particular, watermelon (*Citrullus lanatus*) peel extract has been identified as an effective reducing and stabilizing agent, due to its high content of antioxidant compounds [7] .

Compared to other plant extracts used in the synthesis of nanoparticles, such as the alcoholic extract of eucalyptus (*Eucalyptus globulus*) or the aqueous extract of papaya (*Carica papaya*), watermelon peel extract offers significant advantages. Its availability, low cost, and high concentration of antioxidants position it as a competitive alternative [8]. While eucalyptus extract has shown favorable results in terms of nanoparticle stability, and papaya extract is effective in reducing metal ions, watermelon extract combines these properties with a higher adsorption capacity, thanks to the synergistic interaction of its phenolic compounds [9].

Studies have shown that the use of plant extracts not only improves the stability and functionality of nanoparticles but also contributes to the circular economy by valorizing agro- industrial waste. This approach enables the synthesis of materials with lower energy and environmental costs, promoting sustainable practices in materials science[10]. In this context, NP-FeO-CLs synthesized using watermelon peel extract represent a promising solution to address lead contamination in water sources.

Our main objective of this study is to evaluate the efficiency of NP-FeO-CL in the removal of Pb ions from aqueous solutions under different experimental conditions. In addition, the fitting of the experimental data to isotherm and adsorption kinetics models will be analyzed to better understand the mechanisms involved in the process [11]. The findings of this research could lay the foundation for the development of accessible and sustainable technologies for the mitigation of heavy metal contamination in various affected regions [12].

2. Materials and methods

2.1. Reagents and materials

Watermelon was collected from the coastal region of Ecuador, province of Manabí, canton Tosagua, from the El Porvenir farm, with coordinates 1◦26′00.8 ″S 80◦21′20.2 ″′W. Iron (III) chloride salts, hexahydrate, and sodium hydroxide were purchased from ISOLAB Laborgerate GmbH, Wertheim, Germany, while iron (II) chloride salts were obtained from LOBA CHEMIE PVT. The

standard lead solution (1000 mg /L) was purchased from AccuStandard in New Haven, Connecticut, U.S.A. All chemicals and solvents used in this study were of analytical grade, and no additional purification system was required. Milli-Q water was used to prepare the solutions (Resistivity: 18.2 MΩ.cm at 298K).

2.2. Methods

2.2.1. Obtaining watermelon extract

The aqueous extract was extracted from watermelon (*C. lanatus*) rinds. The collected peels were dried at 90°C for one week to preserve their quality. Subsequently, a solution was prepared by heating distilled water to 80°C, into which the powder from the dried rinds was added. This mixture was kept at the same temperature for 5 minutes before cooling to room temperature, then filtered and stored in amber glass jars at 5°C for later use in the preparation of the aqueous extract.

2.2.2. Obtaining iron nanoparticles (NP-FeO-CL)

For the synthesis, a solution was prepared by combining ferrous chloride and ferric chloride in deionized water with masses of 0.63 g and 1.62 g, respectively, in a 100 ml volumetric flask and stirred constantly. After 5 min of stirring, 0.8 ml of the watermelon rind extract and 10 g of the prepared rind was added. Then, sodium hydroxide solution was added dropwise until a pH of 10 was reached, continuously monitoring the pH throughout the process. The mixture was left to stand to enable the NP-FeO-CL to settle to the bottom of the beaker. The settled nanoparticles were washed in a centrifuge using 70% alcohol and deionized water, and then dried in an oven at 65 °C for 24 hours.

3. Experimentation

3.1. Characterization studies

A morphological analysis of the magnetite nanoparticles was carried out using a scanning electron microscope (SEM, Tescan). FTIR analysis was performed with a JASCO FT/IR-4100 spectrometer in the range of 4000 to 500 cm^{-1}, recorded in absorbance mode with a resolution of 16 cm^{-1}. UV-Visible measurements were carried out with a spectrometer (Thermo) 200 at a wavelength of 700 nm. All experimental analyses were carried out under experimental conditions and at room temperature.

3.2. Feasibility of the nanoparticle as a Pb retainer in aqueous solutions

To evaluate the lead (II) retention capacity, a certified lead standard at 1000 mg/L was used. From this standard, a stock solution of 2.0 mg/L was prepared, which served as the basis for the preparation of various solutions for the experimental tests. The solutions were put in contact with NP-FeO-CL nanoparticles and, after reaching equilibrium, were filtered. Subsequently, the samples were digested with acid, and the lead concentration was measured by atomic absorption spectrometry, which enabled the calculation of the percentage of lead adsorption on the synthesized particles. A range of initial lead concentrations was explored, varying from 2.0 to 15 mg/L, and a dosage amount of nanoparticles

ranging from 0.05 to 0.5 g was used. In addition, the effect of pH on the adsorption of lead ions was studied by varying the pH in a range from 1.0 to 7.0. To analyze the kinetic behavior of adsorption, aliquots of the solution were taken at 5-minute intervals, which enabled the elaboration of kinetic curves. Experiments were also carried out to determine the adsorption isotherms at an initial concentration of 2.0 mg/L. Finally, the thermodynamic properties of the adsorption process were investigated by three experiments at different temperatures (25, 35, and 45° C), using the same initial concentration of 2.0 mg/L lead.

The flowchart illustrating the synthesis process of NP-FeO-CL is presented below (Figure 1). This diagram provides a clear overview of the stages involved in the synthesis. Additionally, a scheme detailing the synthesis process of NP-FeO-CL and its subsequent adsorption is included (Figure 2), enabling a better understanding of the interactions and mechanisms occurring within this process.

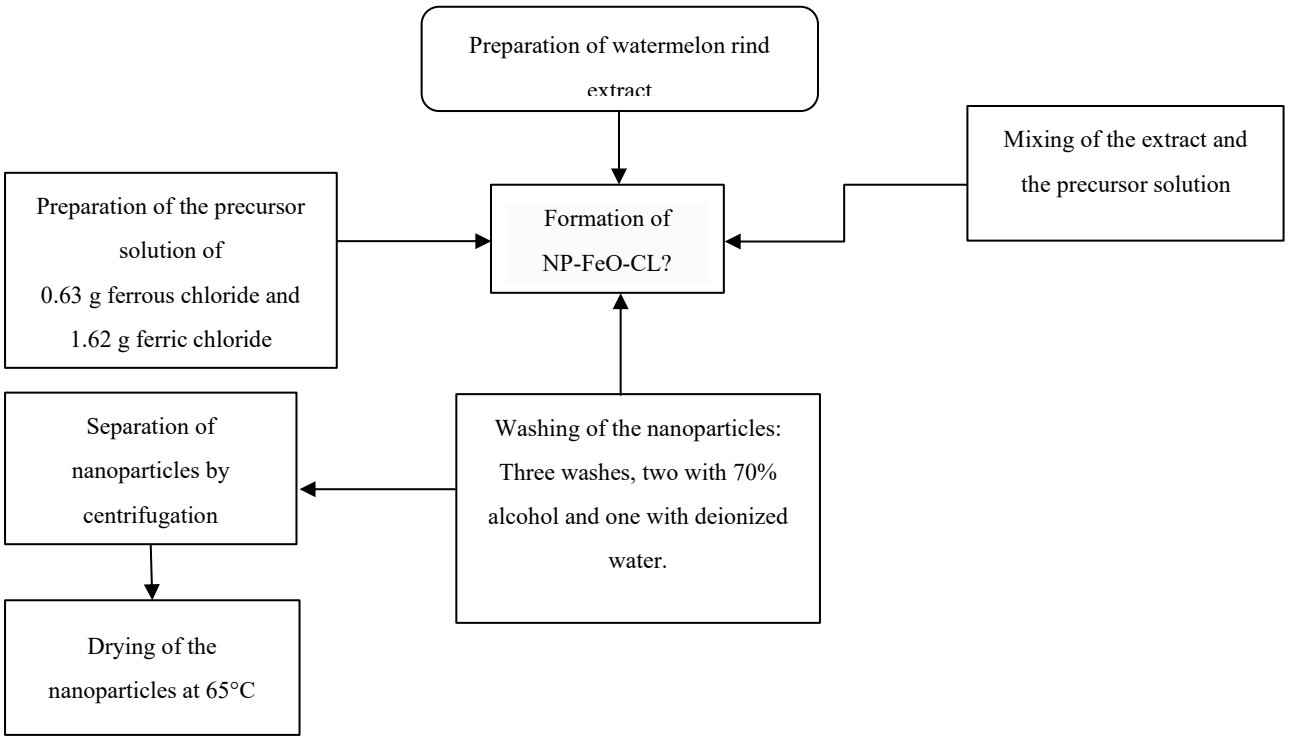

Figure 1. Flowchart diagram of the synthesis of NP-FeO-CL.

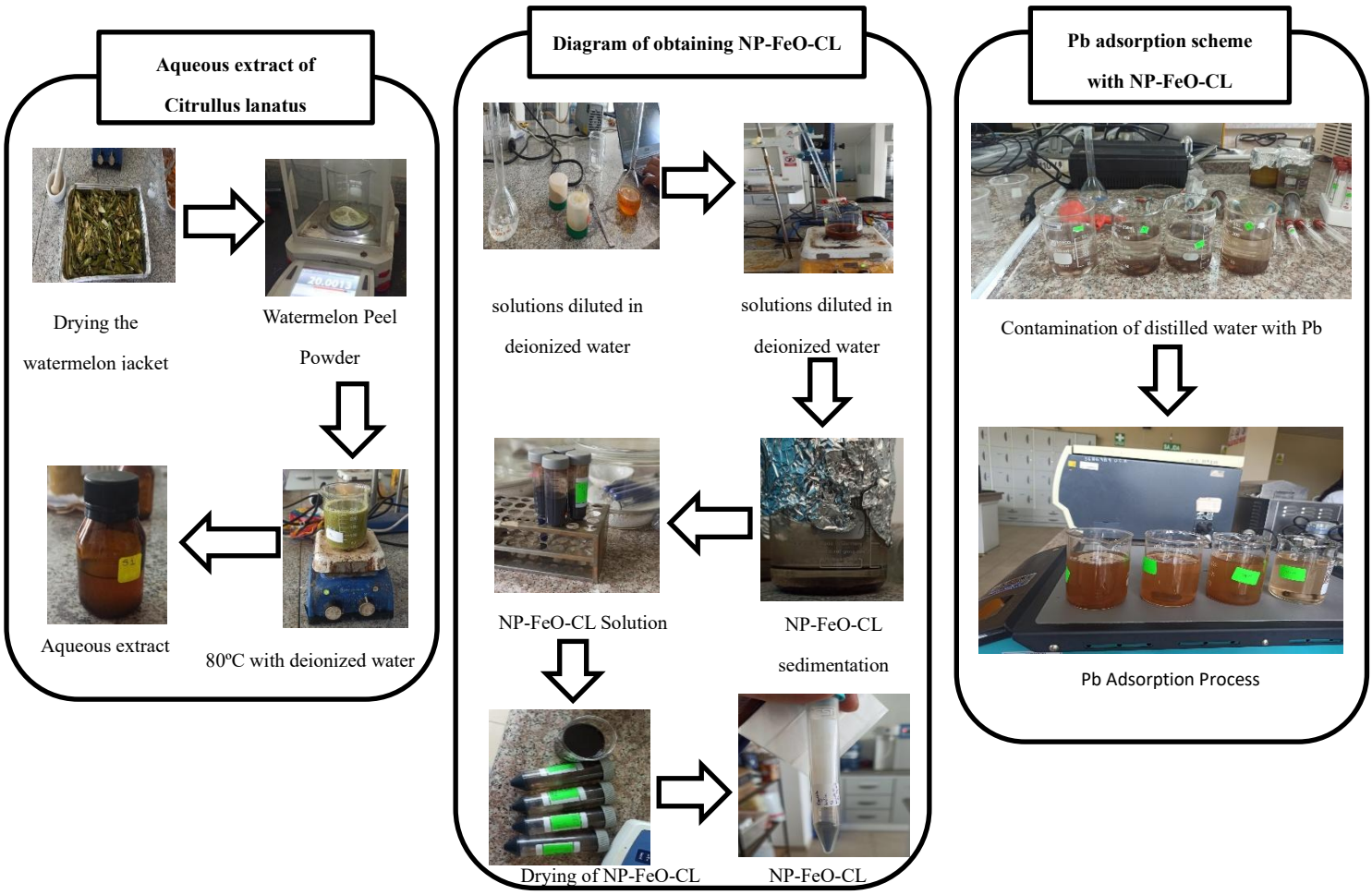

Figure 2. Scheme of the synthesis process of NP-FeO-CL and Adsorption.

4. Results

4.1. Characterization of NP-FeO-CL

4.1.1. Infrared spectroscopy (FT-IR)

The Fourier transform infrared spectroscopy (FT-IR) technique was used to identify the functional groups present in both the *C. lanatus* extract and the synthesized iron oxide nanoparticles. According to the study by De la Cueva F et al [13], the FT-IR spectrum of the watermelon extract showed a peak at 3251.4 cm^{-1} associated with O-H bond stretches, indicative of alcohols, phenols, or water, suggesting the presence of hydroxyl groups or water content in the extract. In addition, a peak at 1612.2 cm^{-1} was observed, suggesting the presence of C=O (carbonyl) or C=C (carbon double bond) groups, which is indicative of phenolic compounds or organic acids. Another relevant peak at 1025.94 cm^{-1} is associated with C-O stretches, typical of sugars, ethers, or alcohols, reflecting the possible presence of sugars such as fructose and glucose. Finally, the peak at 609.39 cm^{-1}, in the fingerprint region, could be related to vibrations of C-H or C-O bonds in complex structures. Compared to the content by Chávez García M L et al. [14], the FT-IR spectrum of the iron oxide nanoparticles revealed a characteristic vibrational band at 566.96 cm^{-1}, corresponding to the Fe-O bond, confirming the presence of magnetite, with

values that coincide with those reported in the literature. Bands were also identified at 3386.39 cm^{-1} and 1627.63 cm^{-1}, corresponding to the hydroxyl (- OH) and carbonyl (-CO) groups, respectively. These results suggest that the carboxyl group (-COO) interacted with the core of the nanoparticles, while the polyphenols present in the watermelon peel extract acted as reducing and stabilizing agents for the magnetite nanoparticles [15].

Comparison between the spectra of watermelon rind and magnetite showed significant differences in their chemical compositions, reflecting the complexity of the organic composition of watermelon rind versus the inorganic structure of magnetite. Although both exhibited bands in the O-H group region, watermelon rind further exhibited bands associated with phenolic compounds and sugars, while magnetite was characterized primarily by Fe-O bond vibrations, underscoring the differences between these two materials, as seen in Figure 3.

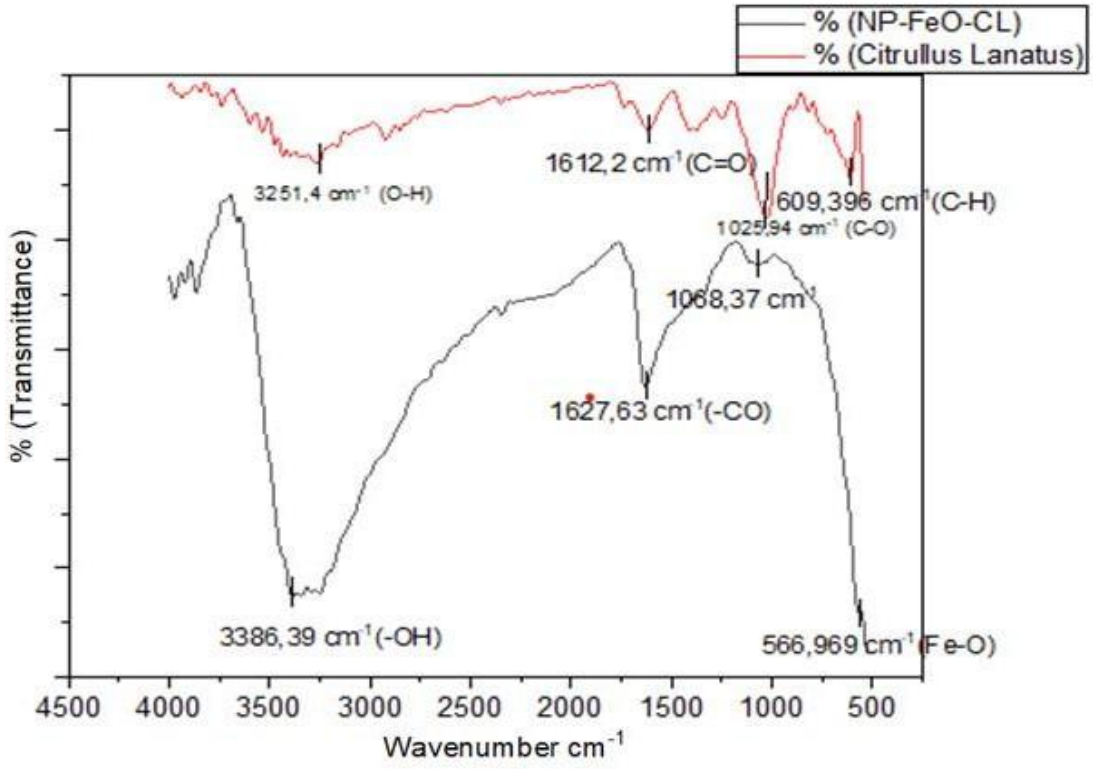

Figure 3. FT-IR of NP-FeO-CL and CL.

4.1.2. UV-Visible Spectroscopy

The UV-Visible absorption spectrum of NP-FeO-CL synthesized from watermelon rinds showed an absorbance peak at 321.45 nm with a value of 0.005 Abs. According to the study by Castillo-Granada A L, et al. [16] , this peak indicated the presence of magnetite nanoparticles, since it was in the typical absorption region for this material.

The gradual decrease in absorbance after this peak suggested a homogeneous distribution in size and morphology, indicating a successful and controlled synthesis. The absence of other significant peaks in the spectrum suggested that the nanoparticles were highly pure, with no evidence of additional phases or contaminants. The overall shape of the spectrum matched the expected optical behavior for

magnetite nanoparticles, confirming the effectiveness of the watermelon peel-based synthesis method, as seen in Figure 4.

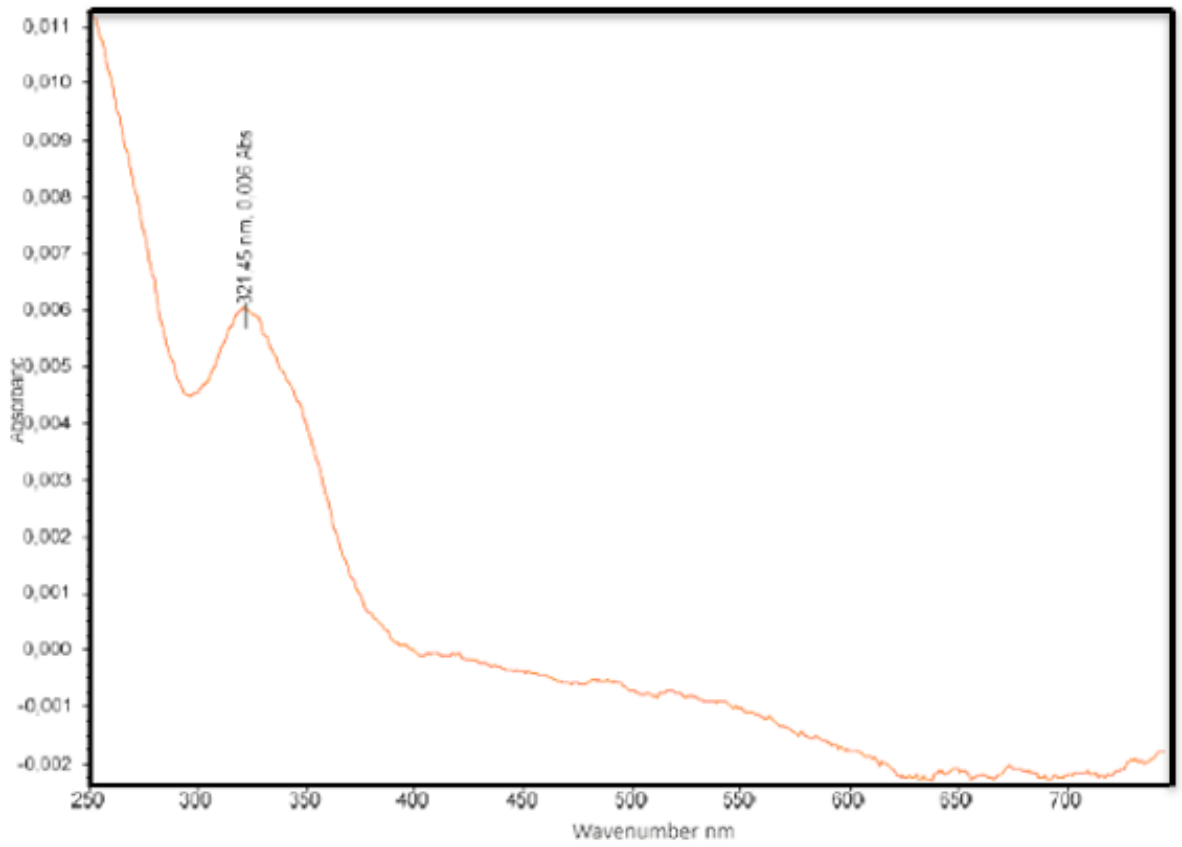

Figure 4. UV-Visible spectrum of NP-FeO-CL (own image from the equipment).

4.1.3. SEM results and EDS analysis of NP-FeO-CL nanoparticles.

Scanning electron microscopy (SEM) was used to measure the size of the nanoparticles. The maximum scale reached was 2 µm, and the presence of micro- and nanoparticles of NP- FeO-CL was observed. Figure 5 shows that scale A corresponds to 2 µm and scale B to 5µm. The smallest particle size was determined using the Image software, which made it possible to identify and, despite the limitations of the equipment, a significant number of microparticles and nanoparticles were detected, confirming the presence of NP-FeO-CL [17]. One of the smallest particles had a size of 0.070 µm, equivalent to 70 nm, which fit the definition of nanoparticles, which encompasses sizes between 1 and 100 nm [18].

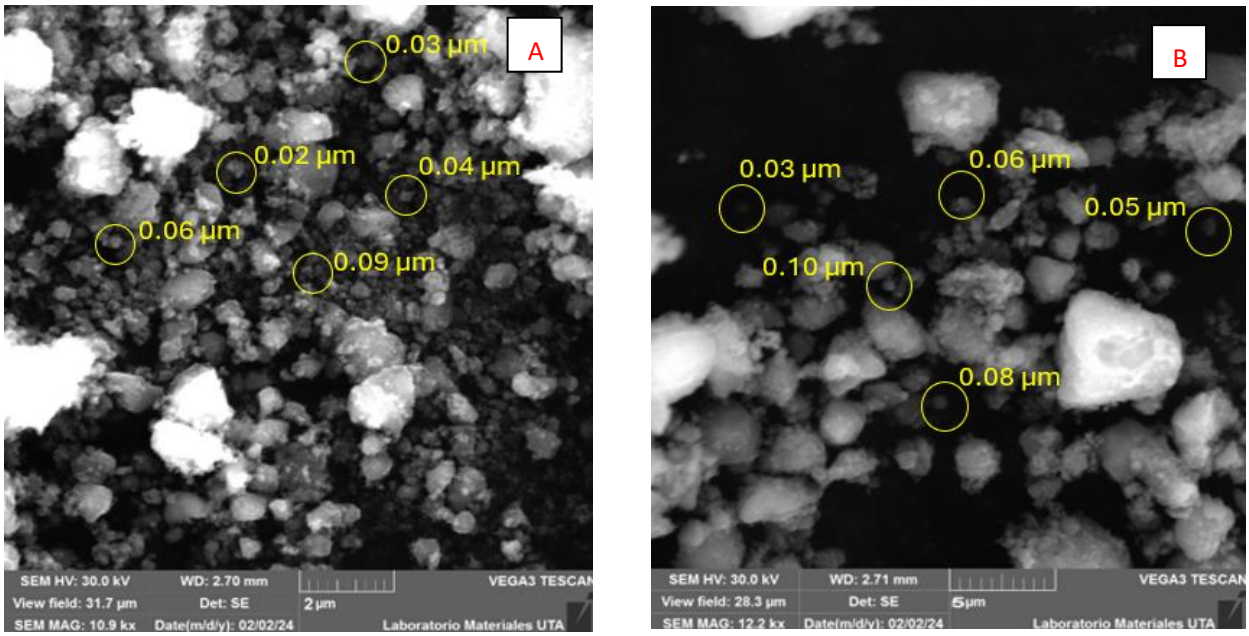

Figure 5. SEM analysis of NP-FeO-CL a different scale. A: 2 µm. B: 5 µm.

The EDS analysis of the NP-FeO-CLs is presented in Figure 6, namely, the area analyzed (Figure 6A) and its spectrum (Figure 6B). In addition, X-ray energy dispersive analysis (EDS) was performed to determine the elemental composition of the nanoparticles [19]. The results of the EDS spectra revealed major peaks corresponding to iron (Fe) and oxygen (O), confirming the presence of iron oxide as the main component of the NP-FeO-CLs. The absence of significant impurities supports the purity of the synthesized nanoparticles. This analysis, in combination with SEM observations, provides a comprehensive characterization of the NP-FeO-CLs, highlighting their potential for environmental remediation applications [20].

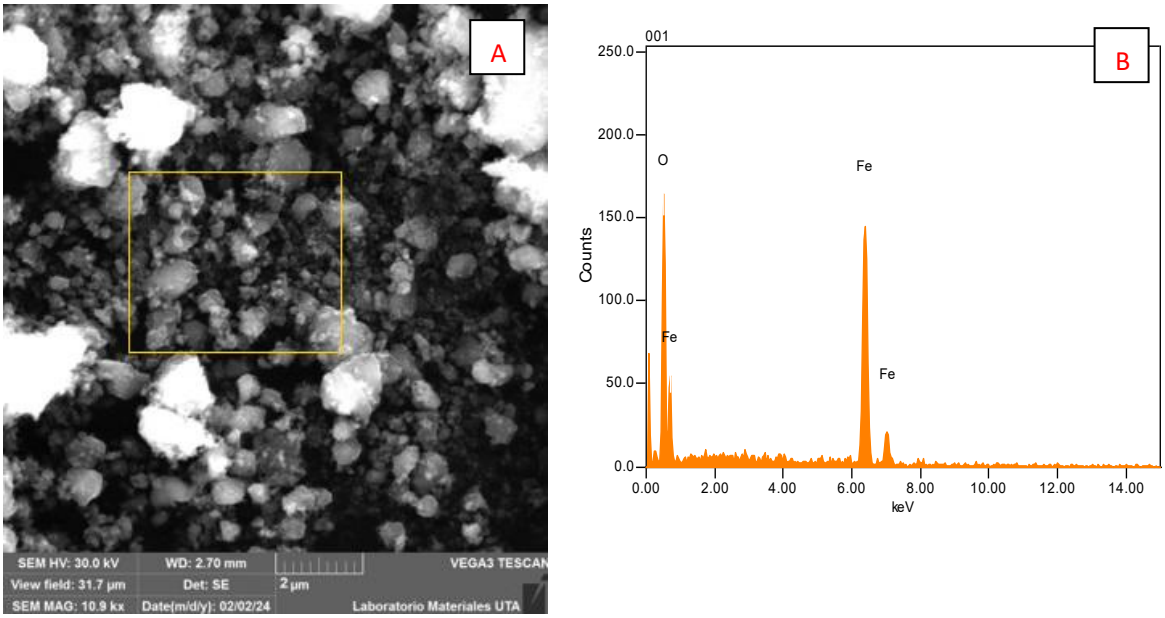

Figure 6. SEM–EDS analysis of NP-FeO-CL: (A) analyzed area and (B) corresponding spectrum.

4.1.4. SEM and EDS analysis after Pb adsorption

The SEM analysis performed after the Pb adsorption process showed that the iron oxide nanoparticles functionalized with *C. lanatus* (NP-FeO-CL) remain present and keep their major characteristics. Images obtained with 5 µm and 10 µm scales showed that the particles maintained their uniform morphology, being predominantly spherical or nearly spherical. Furthermore, although some signs of aggregation were observed, the nanoparticles remained distinguishable and structurally intact.

Regarding dimensions, the initial measurements of NP-FeO-CL taken in images with 2 µm and 5 µm scales showed sizes ranging from 0.05 µm to 0.15 µm. After the adsorption process and considering the present images with 5 µm and 10 µm scales, a slight increase in the average particle size was observed, with values varying between 0.1 µm and 0.75 µm for the 5 µm scale (Figure 7A), and between 0.25 µm and 1 µm for the 10 µm scale (Figure 7B). This increase in dimensions could be attributed to the formation of a Pb surface layer or chemical interaction processes between the metal and the functional groups of the nanoparticles. EDS analysis (Figure 8) supported these observations by confirming the persistence of the major elements, iron (Fe) and oxygen (O), in the particles. The peaks corresponding to these elements indicated that the core of the NP-FeO-CLs were not significantly altered, demonstrating that the nanoparticles remained stable and functional after the adsorption process. Although no clear Pb peaks were identified in this analysis, this could be due to a heterogeneous distribution of the adsorbed metal or the need for further analysis in specific areas.

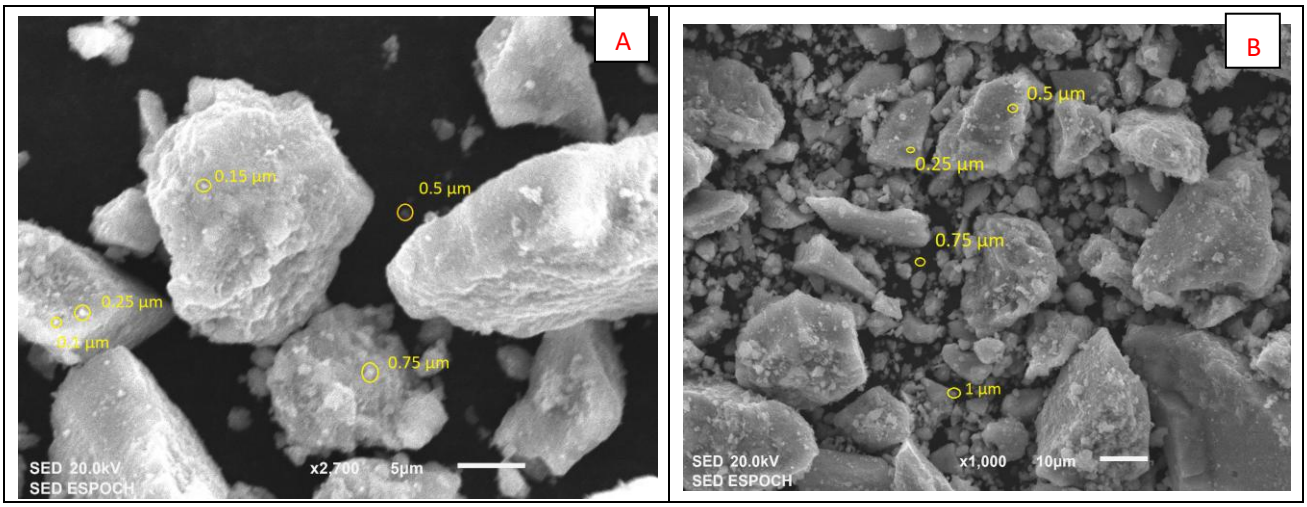

Figure 7. SEM analysis of NP-FeO-CL after Pb adsorption at different scales: (A) 5µm and (B)10 µm.

SEM images and EDS data confirmed that the NP-FeO-CLs remained present after the Pb adsorption process, maintaining their structure and functionality. The slight variation in particle size suggested a successful interaction with the metal, probably through the formation of a surface layer. These results demonstrated that NP-FeO-CLs were effective and stable as adsorbent agents in this context, with no evidence of significant degradation after interaction with Pb.

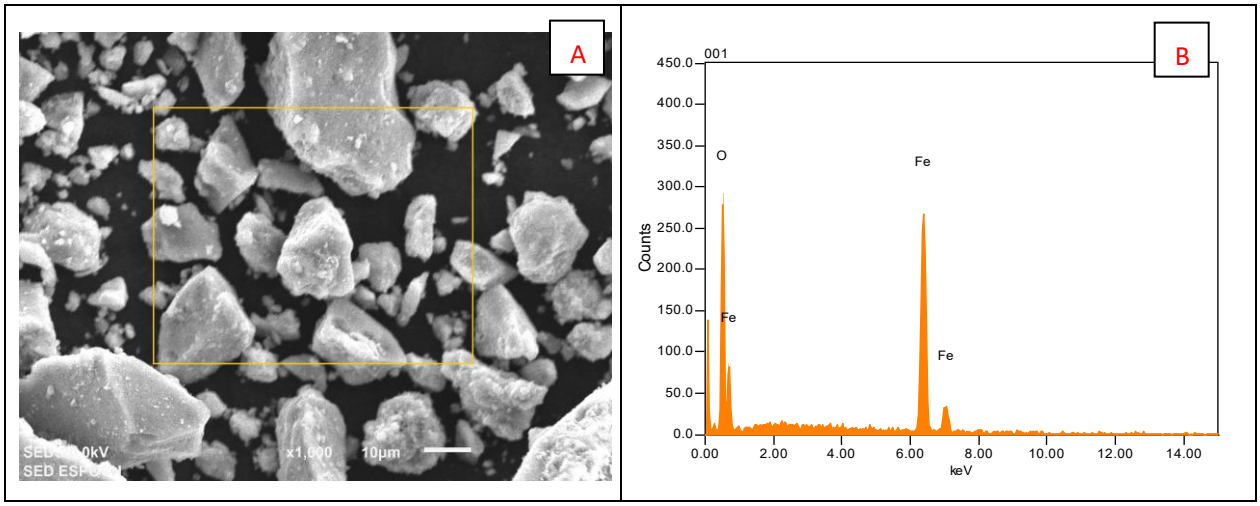

Figure 8. EDS analysis of NP-FeO-CL after Pb adsorption.

Comparison between SEM and EDS analysis before and after the Pb adsorption process showed that the NP-FeO-CLs retained their structure, uniform morphology, and functionality as adsorbent agents. The slight changes in particle size observed in SEM were attributed to the interaction with Pb, while EDS data confirmed that the main core of the nanoparticles remained unchanged, with no signs of degradation. The absence of detectable Pb signals in EDS may be due to the low concentrations employed (ppm), demonstrating the need for complementary techniques to characterize adsorbed trace elements. These results highlight the stability and effectiveness of NP-FeO-CL for environmental remediation applications.

4.1.5. FTIR analysis after adsorption of Pb

The following analysis compares the FT-IR spectra of *C. lanatus* functionalized iron oxide nanoparticles (NP-FeO-CL) before and after lead adsorption. In the region around 3380-3370 cm^{-1}, corresponding to the stretching vibrations of the -OH groups, a shift from 3386.39 cm^{-1} (before adsorption) to 3370.96 cm^{-1} (after adsorption) was observed. This shift suggested interactions between the -OH groups of the nanoparticles and the lead ions, possibly through hydrogen bonding or coordination. The band located around 1630 cm^{-1}, associated with C=O or C=C vibrations, showed a shift from 1627.63 cm^{-1} (before adsorption) to 1639.2 cm^{-1} (after adsorption). This shift indicated possible structural modifications or interactions between the carbonyl or aromatic groups of the nanoparticles and the lead ions. In the region near 1088.37 cm^{-1}, attributed to C-O vibrations, the band present before adsorption was not detected after the process. This suggested that the groups responsible for this vibration actively participated in the interaction with lead, altering its original configuration [21].

Finally, in the low frequency region (<600 cm^{-1}), characteristic of Fe-O vibrations, the band at 566.969 cm^{-1} before adsorption was still visible, indicating that the inorganic structure of the nanoparticles remains intact after adsorption [21].

Overall, the observed changes in the FT-IR spectra suggested that the functionalized nanoparticles effectively interacted with lead ions, mainly through organic functional groups such as -OH, C=O, and C-O, while the iron oxide matrix remained stable. This confirmed the functionalization and

effectiveness of NP-FeO-CLs in the lead adsorption process.

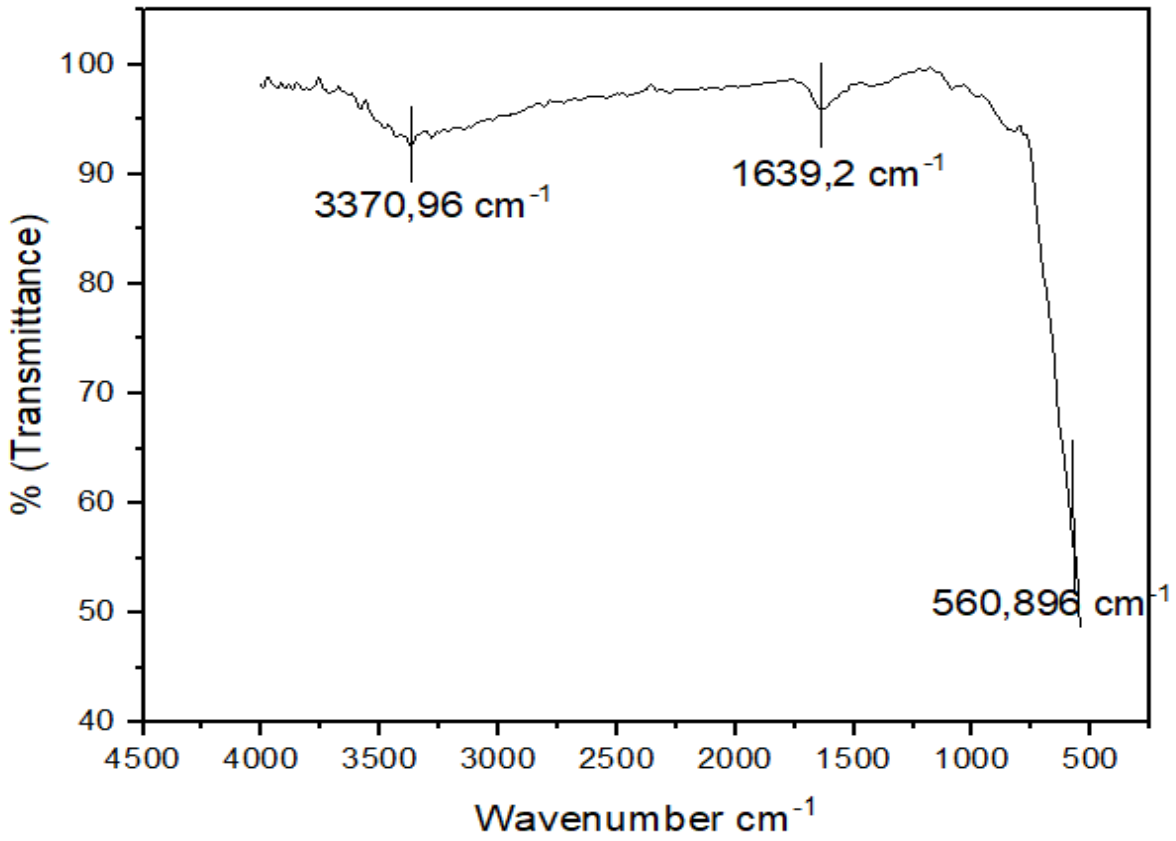

Figure 9. FT-IR of NP-FeO-CL after Pb adsorption.

4.2. Analysis of the Pb removal process

4.2.1. Effect of contact time

To evaluate the influence of time on Pb removal in aqueous solutions, a 2 mg/L solution of deionized water containing a Pb standard was prepared. To this solution, 0.05 g of iron oxide nanoparticles was added and kept in agitation for 5 minutes, taking aliquots every minute. The results showed that in the first minute, 84.21% of the Pb was removed, which was considered a positive result, since any removal above 70% was considered effective. At the end of five minutes, removal reached 91.40%. These results are comparable and optimal in relation to other studies [22], suggesting that the material used is effective for Pb removal in the time evaluated. In Figure 10, the results obtained from the contact time are shown.

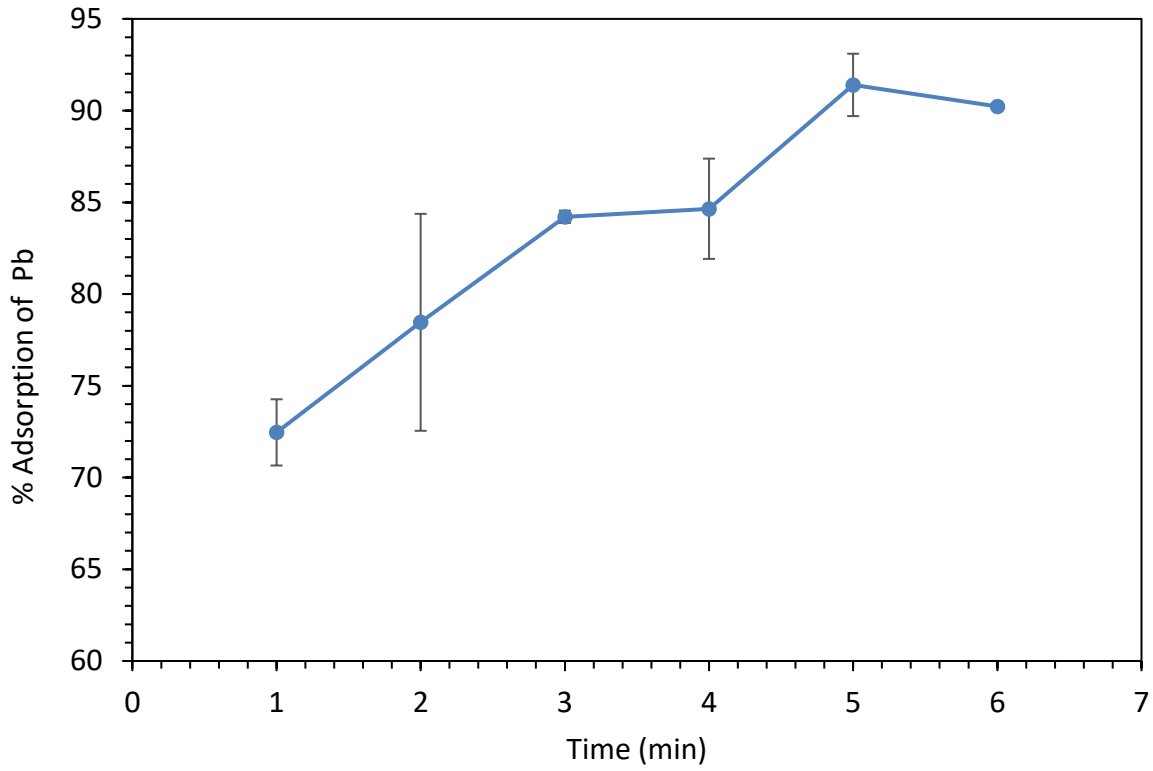

Figure 10. Relationship of time with Pb removal. Test conditions: 2 mg/L; 150 rpm; T=25 ºC; V=100 ml; adsorbent mass = 0.05 g.

4.2.2. Effect of adsorbent quantity

The effect of the adsorbent dosage of NP-FeO-CL on the removal of Pb from aqueous solutions with an initial concentration of 2 mg/L was investigated. Dosages of 0.01, 0.05, 0.1, and 0.5 g of the nanomaterial were evaluated under constant stirring for 5 minutes. The results revealed a non-linear relationship between the adsorbent mass and removal efficiency. A maximum efficiency of 91.40% was achieved with a dosage of 0.05 g. However, upon increasing the dosage to 0.1 g and 0.5 g, the efficiency markedly decreased to 72.49% and 36.10%, respectively (Figure 11). This behavior suggested that beyond an optimal concentration, the excess nanoparticles tend to agglomerate or aggregate. This phenomenon reduces the active surface area available for Pb adsorption, thereby diminishing the overall process efficiency [23].

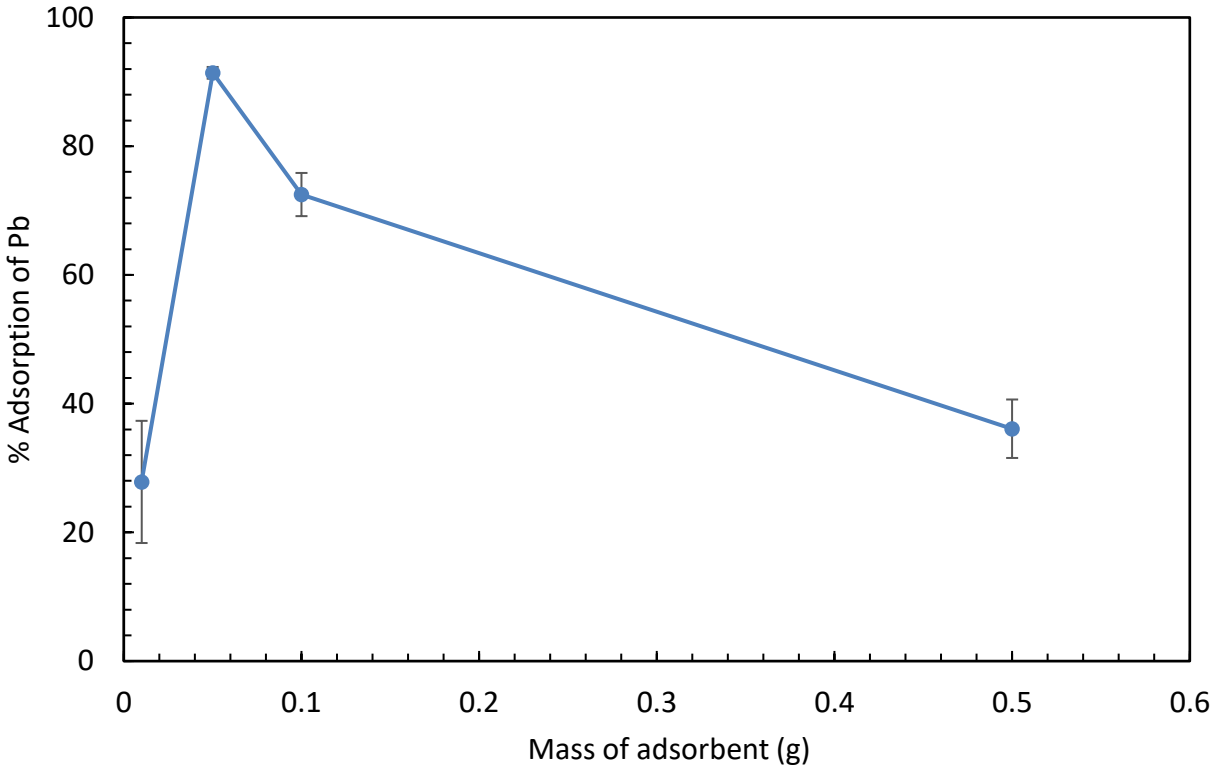

Figure 11. Relationship between the amount of NP-FeO-CL and Pb removal, Test conditions: 2 mg/L; 150 rpm; pH = 4; T=25 ºC; V=100 ml; t = 5 min.

4.2.3. Effect of pH

How pH affects Pb removal in aqueous solutions was investigated by experimenting with 4 solutions of 2 mg/L deionized water containing a Pb standard. The pH values were adjusted to 1 and 3 by the addition of HCl, and to 5 and 7 by the addition of 1 M NaOH.

Under extremely acidic conditions, with a pH of 1, Pb removal was very low, reaching only 7.16%. This was probably due to the decrease in the loading of the iron oxide nanoparticles and the formation of precipitates, which reduced the availability of active sites for adsorption. At pH 3, the removal was slightly improved, reaching 42.47%. At pH 4, the removal increased significantly, reaching 91.40%, indicating that this level of acidity is optimal for Pb adsorption on iron oxide nanoparticles. However, when increasing the pH to 7 by adding NaOH, the removal efficiency decreased, obtaining a maximum of 68.78%, suggesting that it is not as effective in more neutral conditions. In addition, the zero charge point of the adsorbent was analyzed, which was at 11.5, evidencing that the efficiency of iron oxide nanoparticles does not depend on the point of zero charge (PZC), but on the electrostatic forces of magnetite [24]. In Figures 12 and 13, the obtained pH results are shown.

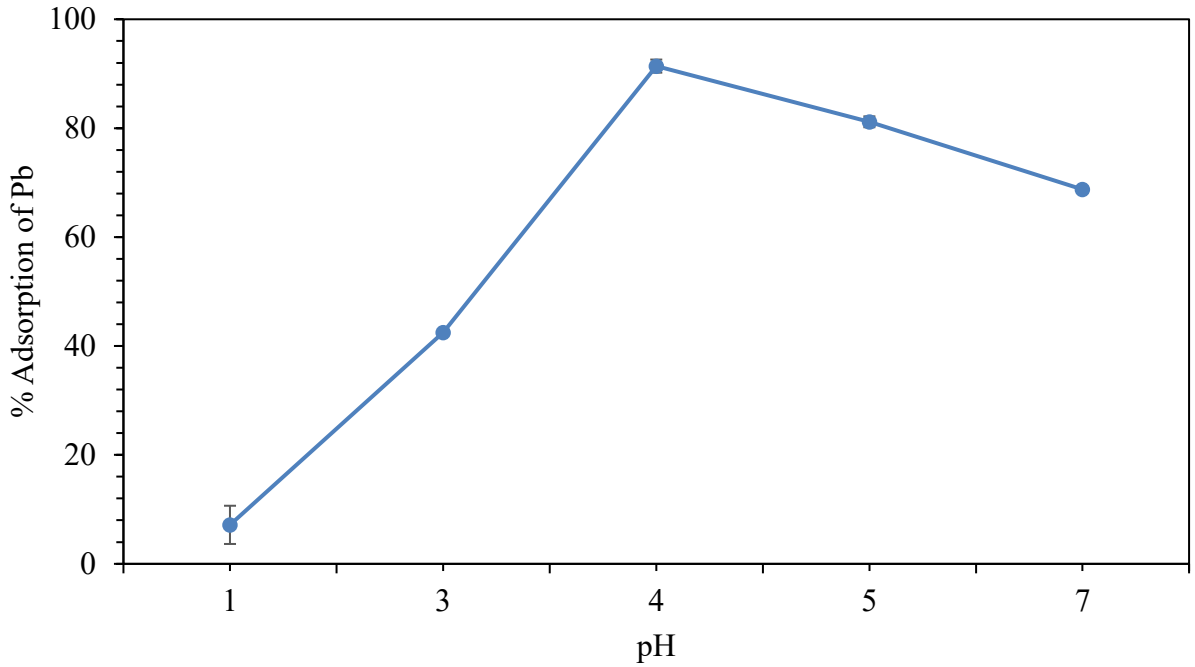

Figure 12. Effect of pH. Test conditions: 2 mg/L; 150 rpm; T=25 ºC; V=100 ml; t = 5 min.

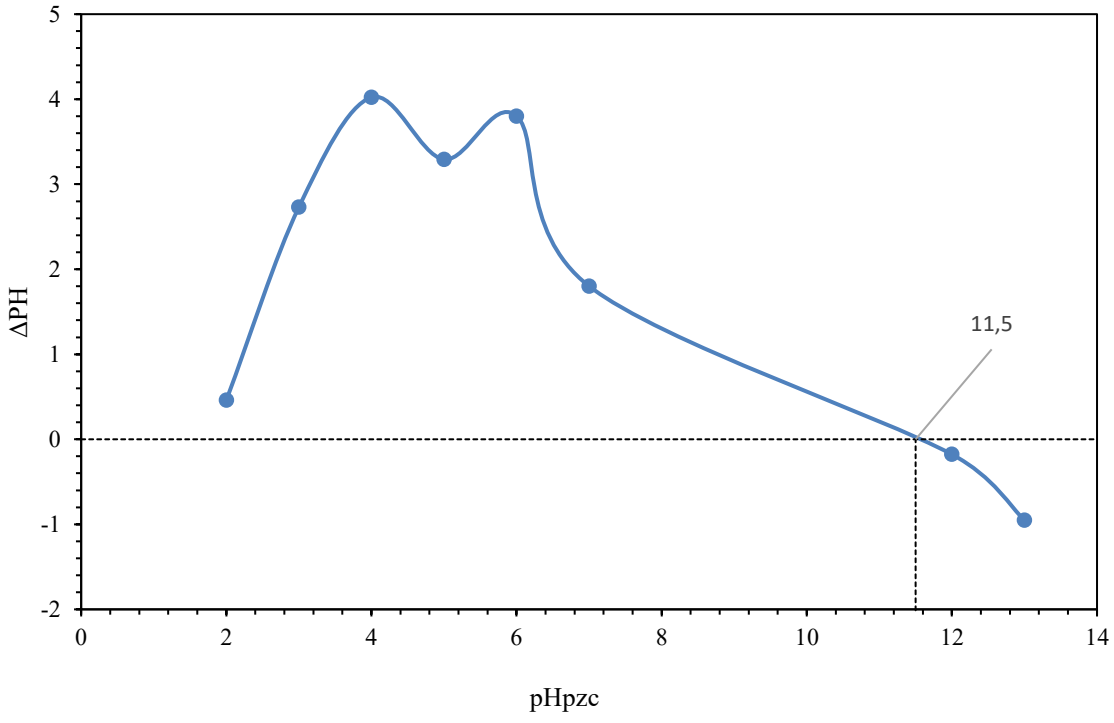

Figure 13. PZC. Test conditions: 2 mg/L; 150 rpm; T=25 ºC; V=100 ml; t = 5 min.

4.2.4. Effect of Temperature

We aimed to determine the optimal experimental parameters for Pb retention using NP-FeO-CL

revealed that temperature has a significant impact on the removal efficiency. At 25 °C, 91.40% Pb removal was achieved while increasing the temperature to 35 °C and 45 °C, the efficiency decreased to 84.79% and 81.79%, respectively. These results, compared with the data presented in the study by Xu W, et al. [25], suggest that the removal at these temperatures is still quite efficient. This behavior indicates that Pb adsorption on the surface of NP-FeO-CLs is most effective at moderate temperatures. At higher temperatures, the particles may have higher mobility and kinetic energy, which reduces the adsorption affinity between nanoparticles and Pb ions. In addition, alterations in the structure of the nanoparticles or additional chemical reactions may occur that affect the efficiency of the process. Figure 14 shows the results of the temperature effect.

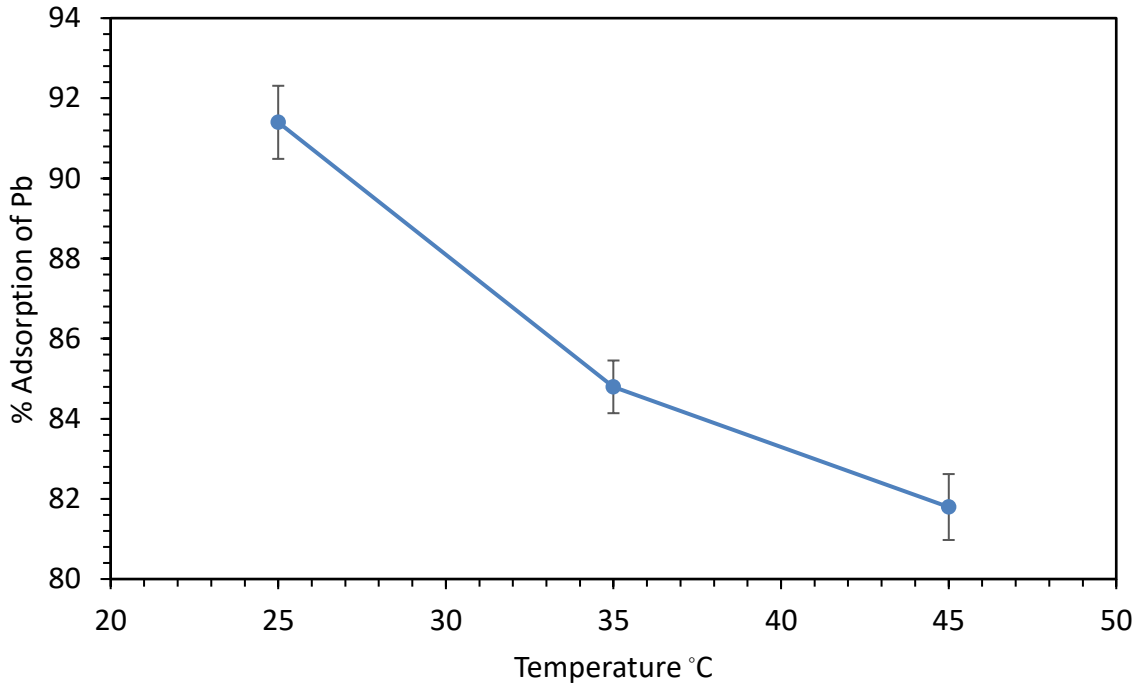

Figure 14. Effect of temperature. Test conditions: 2 mg/L; 150 rpm; V=100 ml; t = 5 min.

4.2.5. Effect of the initial amount of Pb

The influence of the initial concentration of Pb on the removal efficiency was evaluated with contractions of 2, 3, 4, 5, 7, 10, and 15 mg/L. It was observed that when the initial concentration was 2 mg/L, the removal efficiency was 91.40%, which represents the highest value recorded. When increasing the initial concentration to 4 mg/L, the efficiency decreased to 81.58%, and at 10 mg/L, it decreased even more to 65.94%. However, when increasing the initial concentration to 15 mg/L, the efficiency increased slightly to 66.73%, showing that the adsorption of the nanoparticle was not completely saturated compared with [26]. These results indicated that Pb adsorption on NP-FeO-CL is more effective at moderate initial concentrations, which could be due to a saturation of the active sites of the nanoparticles at lower concentrations and an increase in the availability of Pb ions to adsorb at higher concentrations. Figure 15 shows the results of the effect of the initial amount of Pb.

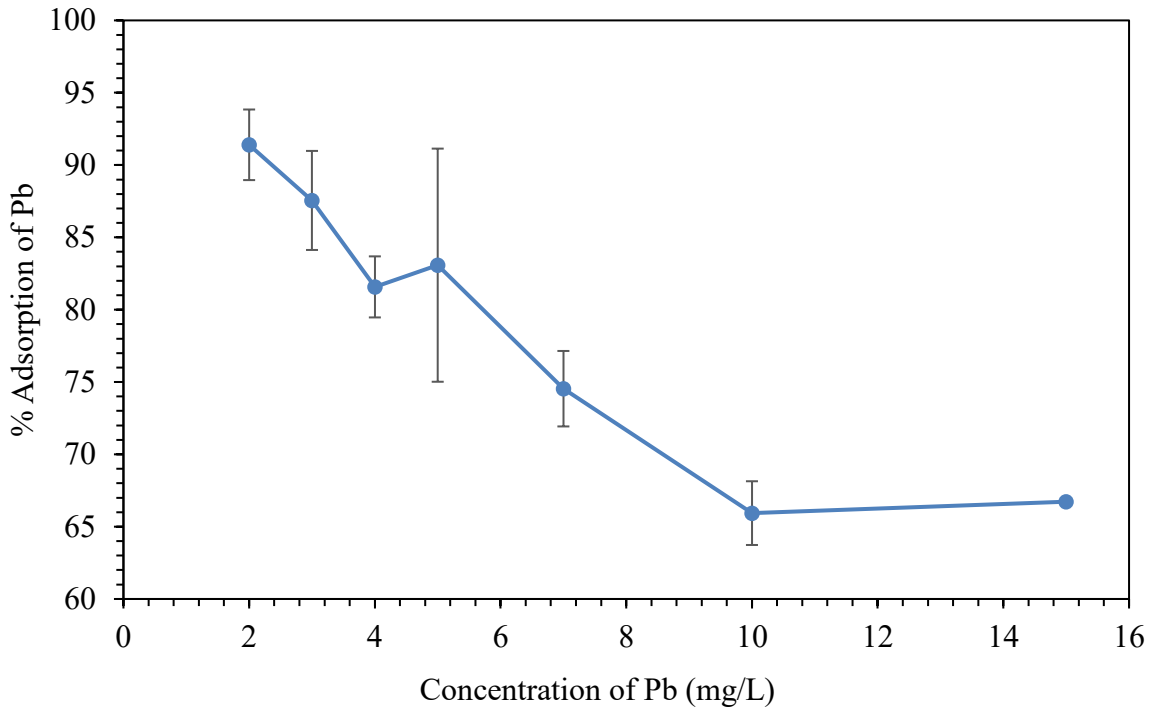

Figure 15. Effect of the initial concentration of Pb. Test conditions: 150 rpm; T=25 ºC; V=100 ml; t= 5 min.

4.3. Adsorption isotherms

Adsorption isotherms were evaluated using the Langmuir, Freundlich, and Temkin models to describe the adsorption of Pb on NP-FeO-CL. In the Langmuir isotherm, the adsorption process was characterized as a homogeneous monolayer on the surface of the adsorbent. It was assumed that all adsorption sites of the adsorbent material possessed equal binding energies, with each site binding to the adsorbate [27] The linearized form of the Langmuir isotherm is expressed as follows:

$$angmuir: \ \frac{Ce}{q} = \frac{1}{q_m \times KL} + \frac{Ce}{q_m} \tag{1}$$

Where q_m represents the maximum sorption capacity expressed in (mg/g), and KL is the Langmuir equilibrium constant (L/mg).

The Freundlich isotherm describes heterogeneous and multilayer adsorption occurring on the porous surface of the adsorbent and is expressed as follows:

$$Freundlich: \ Log\ q = \ Log\ Kf + \frac{1}{n} LogCe \tag{2}$$

Where Kf is the Freundlich constant (mg $^{1-1/n}$ g $^{-1}$ L $^{1/n}$) related to the adsorption capacity and 1/n (dimensionless) is the adsorption intensity.

The Temkin isotherm model takes into account adsorbate interactions, especially for energies higher than those of physical interactions. Unlike other models, the coverage decreased linearly with energy than logarithmically and considered a maximum binding energy [28]. The linear representation of the Temkin

model is expressed as follows:

$$Temkin:\ \ qe = \frac{RT}{b_T} Ln\, A_T + \frac{RT}{b_T} LnCe \tag{3}$$

Where RT/bT (J mol^{-1}) represents the Temkin constant associated with heat of sorption, while A (L g^{-1}) is the equilibrium binding constant. R (8.314 J mol^{-1} K^{-1}) is the universal gas constant, and T (K) denotes the absolute temperature of the solution.

According to the results obtained, the Freundlich model fitted more accurately to the experimental data, showing an adsorption capacity KF = 16.99 mg/g and a correlation coefficient R2 = 0.94. This suggests that the adsorption follows a multilayer trend, indicating greater flexibility in the adsorption process and reflecting the heterogeneity of the nanoparticle surfaces [29]. Furthermore, the heterogeneity factor n resulted in a value of 1.97 L/mg, and since the value of n is greater than 1, it is concluded that the adsorption is physical between Pb ions, and the surface of their NP- FeO-CL is favorable [30]. On the other hand, the Langmuir model presented a lower correlation coefficient R2 = 0.77 and a calculated maximum adsorption capacity of qm = 47.16 mg/g. The Temkin model applied to adsorption yielded an equilibrium constant AT = 7.93 L/g, indicating a significant affinity between the adsorbent and the adsorbate, while the value of bT = 259.10 J/mol suggested considerable adsorption energy; however, desorption may also occur. Nevertheless, the coefficient of determination R^2 = 0.78 indicated a moderate fit of the model to the experimental data, suggesting that although the adsorption process involves interactions between the adsorbent and the adsorbate, the Temkin model may not fully capture its behavior [31]. The higher coefficient of the Freundlich constant reinforced the suitability of this model for the specific system [32], as shown in Table 1 and in Figures 16, 17, and 18, and the results obtained in the Langmuir, Freundlich, and Temkin models are shown.

Table 1. Langmuir, Freundlich, and Temkin models.

Langmuir Model			Freundlich model		
q_m *(mg/g)*	*KL (L/mg)*	R^2	*Kf (mg/g)*	*n (L/mg)*	R^2
47.16	0.64	0.77	16.99	1.97	0.94
Temkin Model					
A_T*(L/g)*		b_T *(J/mol)*		R^2	
7.93		259.10		0.78	

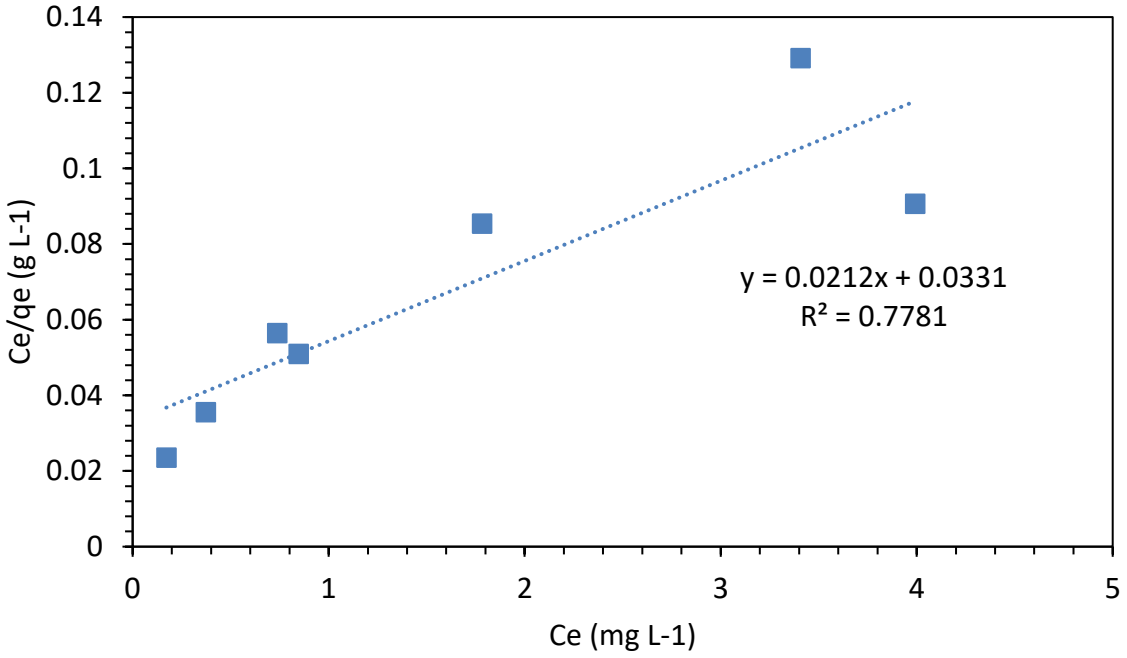

Figure 16. Pb (II) adsorption isotherms on NP-FeO-CL according to the Langmuir model.

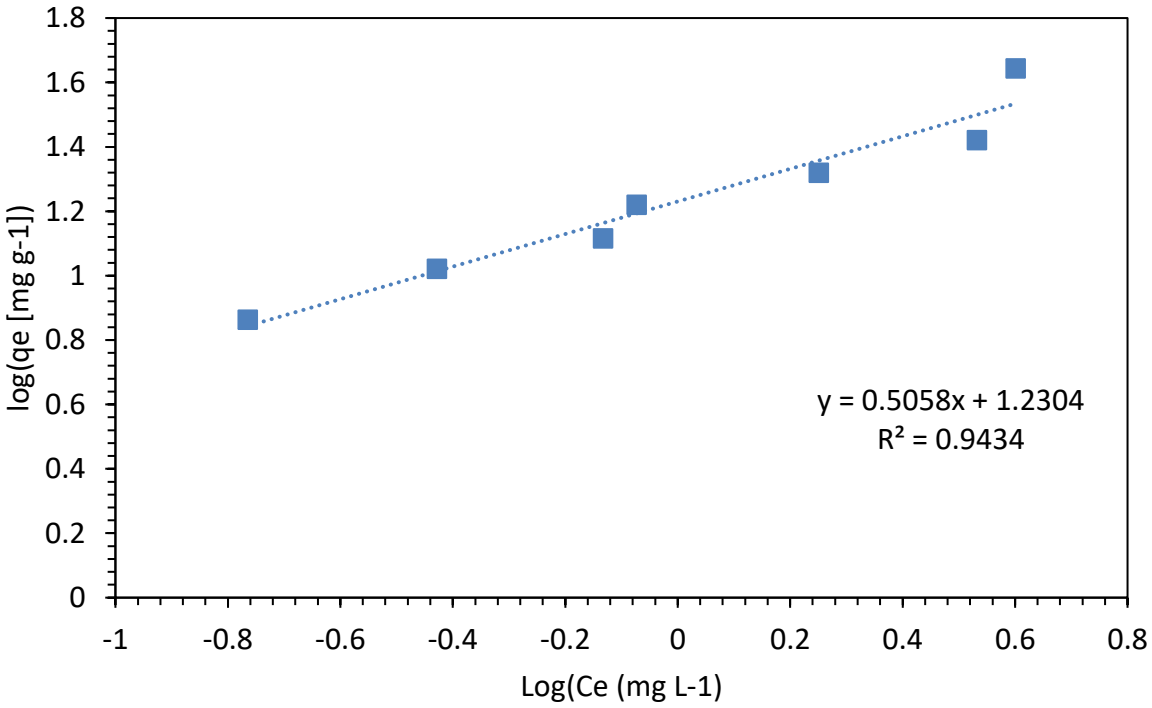

Figure 17. Pb (II) adsorption isotherms on NP-FeO-CL according to the Freundlich model.

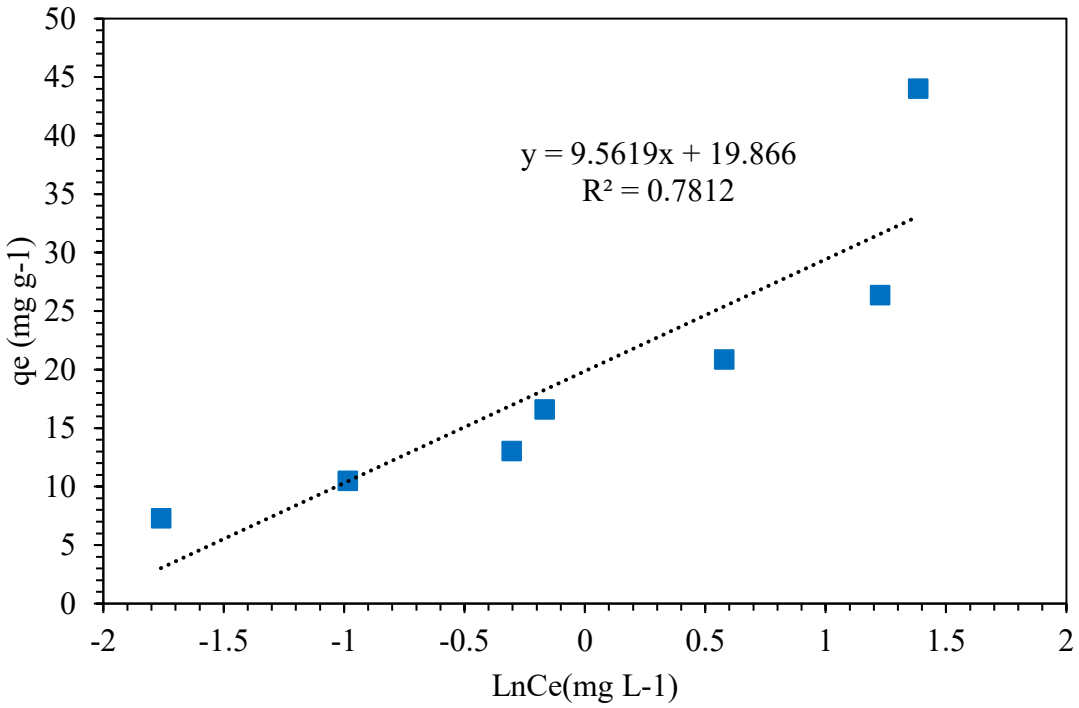

Figure 18. Pb (II) adsorption isotherms on NP-FeO-CL according to the Temkin model.

4.4. Adsorption kinetics

The adsorption kinetics of Pb on NP-FeO-CL was studied using pseudo-first-order, pseudo-second-order, and Elovich kinetics models. The pseudo-first-order linear model can be expressed as follows:

$$\ln(q_e - q_t) = \ln(q_{e-max} - k_1 t) \quad (4)$$

Where k_1 is the adsorption rate constant (min $^{-1}$), q_e (mg/g) is the adsorption capacity at equilibrium, q_t (mg/g) is the adsorption capacity at time t (min), and $q_{e\text{-}max}$ (mg/g) is the maximum amount adsorbed.

The pseudo second-order model describes the chemisorption process that occurs between vacant sites on the adsorbent surface and the Pb (II) ion [33]. The pseudo second-order linear model is expressed as follows:

$$\frac{1}{q_t} = \frac{1}{q_e} + k_2 t \quad (5)$$

The Elovich kinetics model describes systems where the adsorption rate decreases exponentially with time due to the heterogeneity of the adsorbent surface. This model is particularly useful for describing processes where chemical reactions play an important role in adsorption [34]. The linear form of the model is represented as follows:

$$q_t = \frac{\alpha}{\beta}\ln(\alpha\beta) + \frac{1}{\beta}\ln(t) \quad (6)$$

Where β represents the adsorption constant associated with activation energy of chemisorption (g^{-1} mg), and α is the initial adsorption rate (mg/g.min).

Table 2 and Figures 19, 20, and 21 summarize the kinetic constants obtained in the experiment. A comparison of the R^2 values from both models revealed that the pseudo-second-order model exhibited a superior R^2 of 0.99. This analysis indicated that the adsorption of Pb (II) is a rapid process that effectively utilizes the available sites on the nanoparticles, and it is further influenced by chemical reactions between the metal ions and active sites. Moreover, this phenomenon occurs in chemical reactions between the metal ions and active sites. The rate constants ($K_1 = 0.61$) and the equilibrium adsorption capacity ($q_e = 3{,}87$) were determined from the experimental data and compared with the theoretical values. According to the study by Martini S, et al. [35], it can be confirmed that the pseudo-second-order model adequately describes the adsorption kinetic process in this system. The values obtained from the Elovich model indicated an efficient adsorption process in the studied system. Parameter β, with a value of 2.27 mg/g, represented the maximum amount of adsorbate that could be adsorbed per unit mass of the adsorbent, while the value of α, at 290.89 mg/(g.min), suggested a high initial adsorption rate, indicating that the process occurred rapidly at the beginning [36]. Additionally, the coefficient of determination (R^2) of 0.94 indicated a good fit of the model to the experimental data, suggesting that the adsorption dynamics in this system followed the trends described by the Elovich model.

Table 2. Kinetic Model Parameters.

Pseudo 1st order model			Pseudo 2nd order model			
$q_e(mg/g)$	K_1 (min^{-1})	R^2	K_1 $(gm\ g^{-1}/g)$	$q_e(mg/g)$		R^2
1.05	0.36	0.92	0.61	3.87		0.99
Elovich Model						
B (mg/g)		α mg/(g.min)			R^2	
2.27		290.89			0.94	

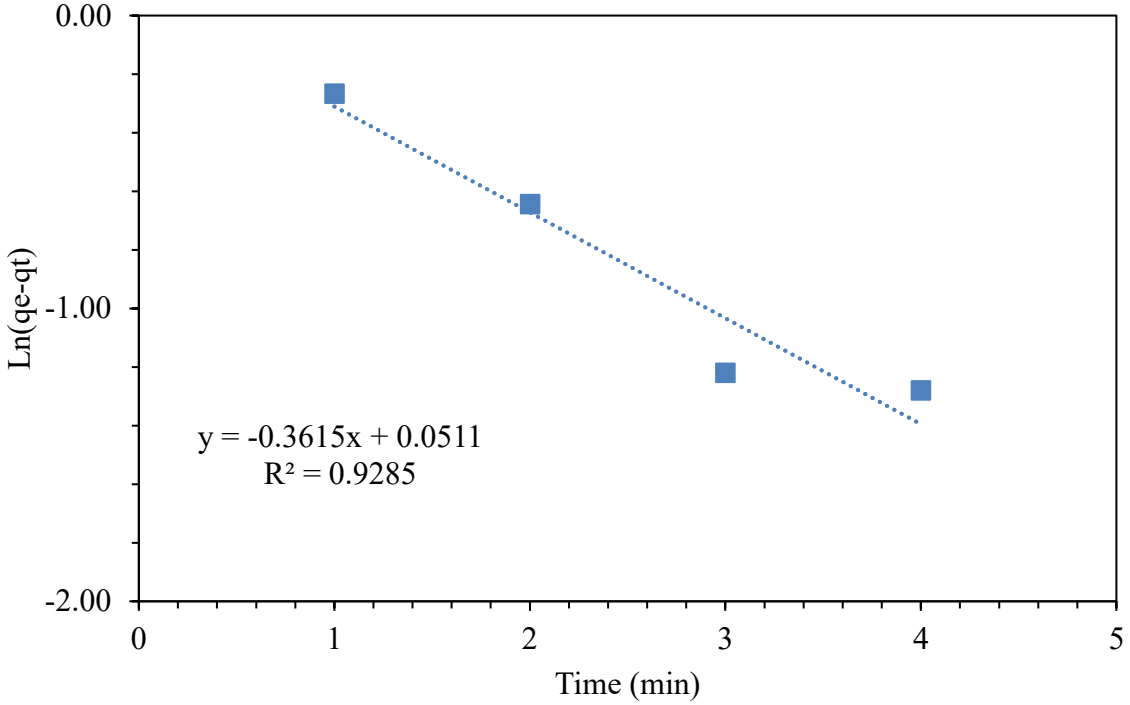

Figure 19. Pseudo first-order kinetic model for Pb removal by NP-FeO-CL.

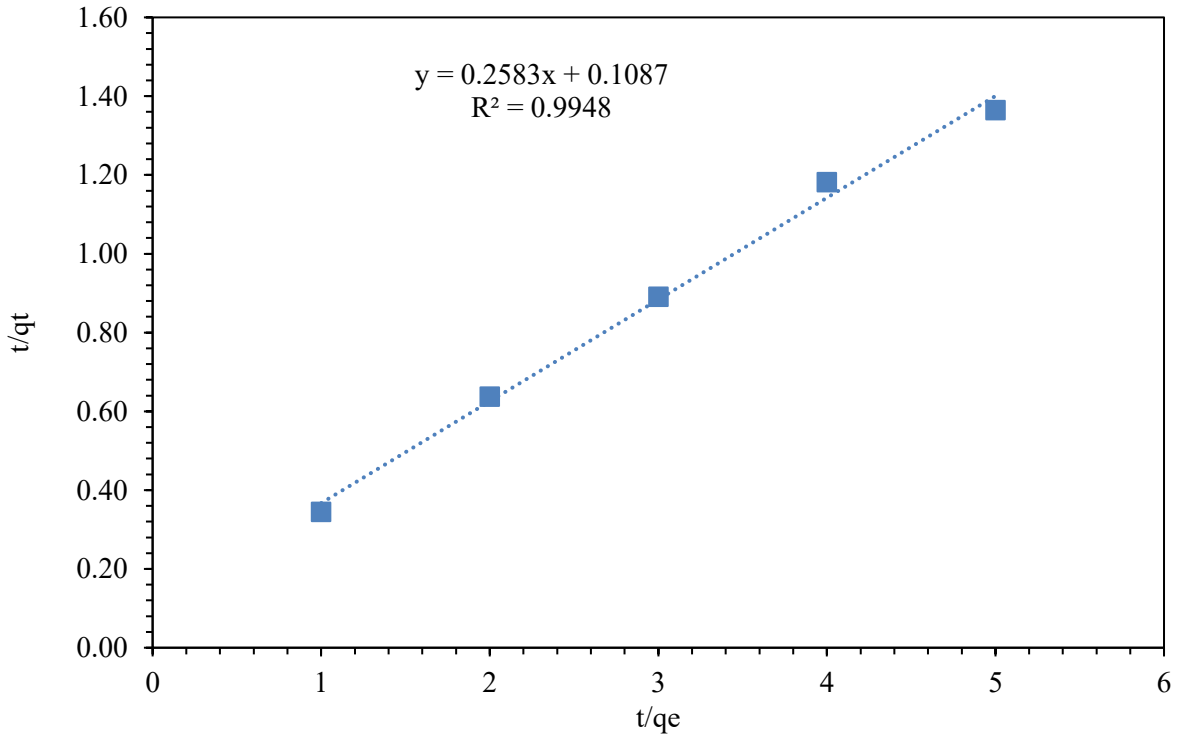

Figure 20. Pseudo second-order kinetic model for Pb removal by NP-FeO-CL.

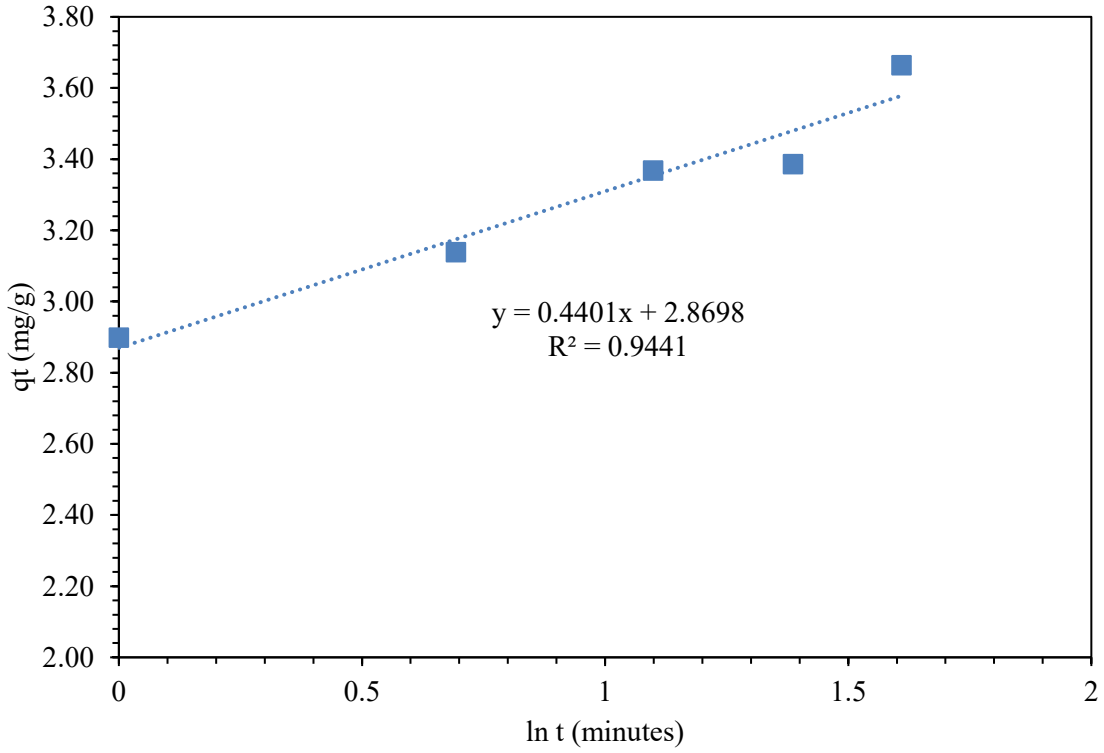

Figure 21. Pseudo second-order kinetic model for Pb removal by NP-FeO-CL.

4.5. Thermodynamic study

The adsorption process implies three essential thermodynamic parameters: Enthalpy ΔHº, entropy ΔSº, and Gibbs free energy ΔGº. These parameters were calculated using the following equations:

$$\Delta G^0 = -RT \ln k_c$$

$$\ln k_c = \frac{\Delta s^0}{R} - \frac{\Delta H^0}{RT}$$

Where R is the ideal gas constant (8.314 J/mol/K) and Kc is the thermodynamic equilibrium constant.

Upon graphing ln Kc versus 1/T, a line with a slope and intercept that enabled the respective calculation of the parameters of ΔHº and ΔSº was obtained. Table 3 presents the results of the thermodynamic parameters. The negative ΔHº value (-45.33 kJ/mol) indicated that the adsorption process was exothermic [37]. On the other hand, the negative values for ΔGº at the three temperatures suggested that the adsorption was spontaneous and energetically favorable. Moreover, the negative ΔSº value (-132.50 kJ/mol · K) suggested a decrease in the level of randomness in the solid-liquid interphase [38]. These results are coherent with the findings [39], where it is reported that the adsorption process for mercury with the adsorbent used is also spontaneous and exothermic.

Table 3. Thermodynamic values for the adsorption of Pb.

Ln Kc	ΔGº (kJ/mol)	ΔHº(kJ/mol^{-1})	ΔSº(kJ)
2.37	-5887.38	-45.33	-132.50
1.71	-4401.86		
1.51	-3945.96		

4.6. Retention capacity in mining water samples fortified with Pb

A study was carried out on samples of water in areas adjacent to mining activities in the Zaruma region, specifically in the VIVANCO Beneficiation Plant. The analyses revealed an extremely acidic pH, with values that oscillated between 2.22 and 2.45. Additionally, the electrical conductivity varied between 1,103 µS/cm and 1,291 µS/cm, surpassing the standard of 1,000 µS/cm, indicating a high concentration of ions in the water. As for the alkalinity, levels of CaCO3 were registered between 0.19 mg/L and 1.76 mg/L, suggesting a possible dissolution of geological matter; these values were considered low compared with the CaCO3 standard of 75 mg/L, according to various studies. Finally, the turbidity level was between 1.09 NUT and 5.17 NUT, indicating a moderate level of suspended particles as sediment or organic matter.

Table 4. Physicochemical parameters and presence of heavy metals in surface waters from the VIVANCO Beneficiation plant (Zaruma-Ecuador).

Physicochemical	Parameters	Unit	M1	M2	M3	M4
Alkalinity		mg/L	1.76	0.25	0.24	0.19
TDS		mg/L	6.47	12.35	6.65	6.62
Conductivity		uS/cm	1103	1291	1199	1189
pH			2.45	2.22	2.26	2.35
Turbidity		NTU	4.36	2.61	5.17	1.09
Heavy metals		*Unit*	*TOTAL*			
Mercurio (Hg)		ug/L	0.77			
Lead (Pb)		ug/L	2.59			
Copper (Cu)		ug/L	0.64			
Chromium (Cr)		ug/L	0.029			
Cadmium (Cd)		ug/L	0.003			

Additional tests were conducted to evaluate the Pb removal capacity in mining water samples collected from the VIVANCO Beneficiation Plant in Zaruma, from El Oro province. The results indicated that the removal efficiency was notably high in the first 5 minutes, reaching 91%. This suggested that the adsorption process for Pb on NP-FeO-CL was very effective in its initial stages, possibly due to the high availability of active sites on the nanoparticles and the rapid interactions between the Pb ions and the nanoparticles in the solution, which can be observed in Figure 22.

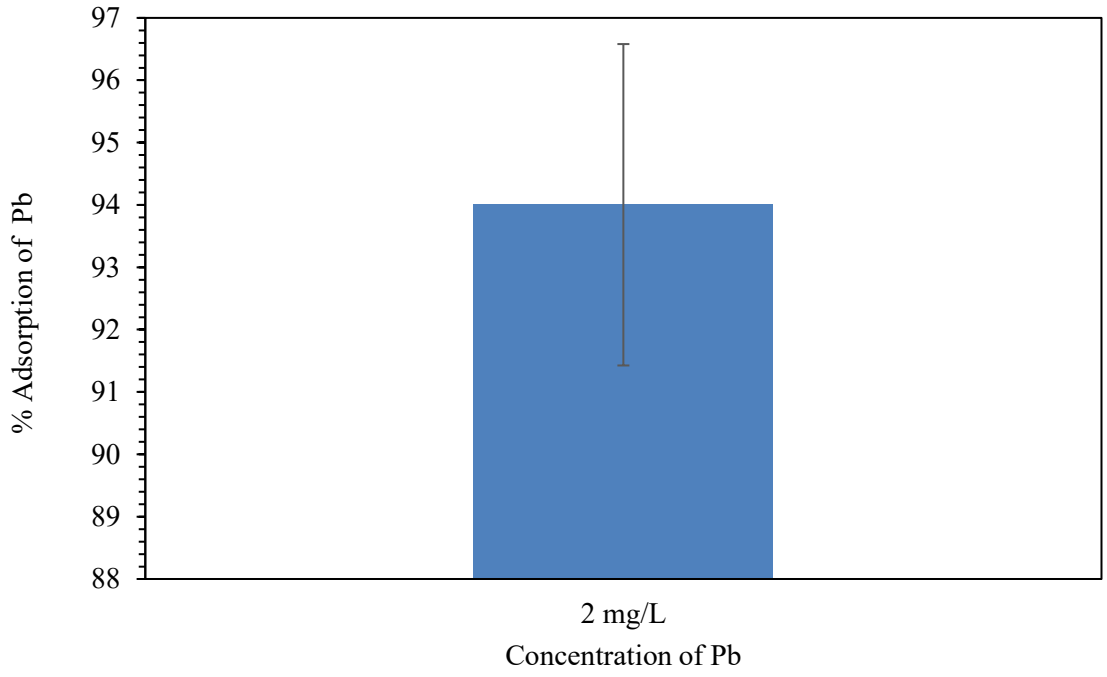

Figure 22. % Adsorption of Pb removal in mining water.

5. Discussion

The results obtained in this study demonstrate the high efficiency of iron oxide nanoparticles functionalizing with watermelon rind extract (NP-FeO-CL) in the adsorption of Pb(II) ions from aqueous solutions. Characterization through FT-IR, SEM, and UV-Visible confirmed the successful formation of the nanoparticles and their structural stability before and after the adsorption process. Spectroscopic analysis revealed the presence of key functional groups that facilitate interaction with Pb(II) ions, explaining the observed retention efficiency [40]. Regarding adsorption capacity, the Freundlich model provided the best fit to the experimental data ($R^2 = 0.94$), indicating a heterogeneous, multilayer adsorption process. This suggests that the active sites on the NP-FeO-CL surface exhibit different adsorption energies, favoring Pb(II) retention. Furthermore, parameter $n > 1$ confirms that the adsorption process is favorable. Although the Langmuir model also showed a good fit ($R^2 = 0.91$), it suggests a monolayer adsorption process, with a maximum adsorption capacity qmax=20.85 mg/g. The Temkin model revealed significant affinity between the adsorbent and the adsorbate, with an AT value of 7.93 L/g and bT of 259.10 J/mol, though its determination coefficient ($R^2 = 0.78$) indicated a moderate fit. This suggests that while interactions between the adsorbent and adsorbate are important, other factors may influence adsorption [41]. On the other hand, the Elovich model showed a good fit to the studied system, with an adsorption constant β of 2.27 mg/g and a high initial adsorption rate α of 290.89 mg/(g.min), confirming that adsorption follows a mechanism that decreases exponentially over time due to the heterogeneity of the adsorbent surface [42]. Kinetic analysis showed that the adsorption process follows a pseudo-second-order model ($R^2 = 0.99$), indicating that the adsorption rate is regulated by the availability of active sites on the adsorbent surface. This implies that the

interaction between Pb(II) ions and NP-FeO-CL is rapid and reaches equilibrium within the first minutes of contact [43]. The thermodynamic study revealed that adsorption is a spontaneous and exothermic process at moderate temperatures (25-35 °C), although its efficiency decreases at higher temperatures. This may be due to possible destabilization of the nanoparticles or desorption of Pb(II) under elevated thermal conditions, suggesting that adsorption is predominantly physical and temperature-dependent [44]. Tests on water samples from mining environments reinforced the applicability of NP-FeO-CL under real conditions. Adsorption efficiencies above 90% were observed within the first minutes of the process, confirming its potential as a fast and effective strategy for the remediation of heavy metal-contaminated water. These findings position NP-FeO-CL as a sustainable alternative for water treatment, promoting the use of low-cost materials with minimal environmental impact [45].

6. Future perspectives

The watermelon rind, a frequently discarded agricultural waste, has found an innovative application in the synthesis of iron oxide nanoparticles (NP-FeO-CL). This approach not only promotes the reuse of an underutilized material but also harnesses the antioxidant compounds present in the rind to enhance the adsorption of heavy metals, such as lead (Pb), in aqueous solutions, achieving a remarkable adsorption efficiency of 93%. Furthermore, these nanoparticles are cost-effective, sustainable, and offer significant advantages compared to conventional technologies. The need to explore solutions like this is becoming increasingly urgent, given the growing issue of water contamination resulting from mining activities and its severe repercussions on the environment and human health. As communities seek sustainable and accessible alternatives, it is essential to continue researching and optimizing the use of natural materials, such as watermelon rind. These investigations will not only improve the effectiveness of water treatment processes but also stimulate the economic development of producing regions, such as Ecuador, thereby promoting a comprehensive approach to sustainability and environmental responsibility.

7. Conclusions

This study demonstrates that NP-FeO-CL is a highly efficient and sustainable tool for the removal of Pb(II) from aqueous solutions. Its adsorption capacity, best fitted to the Freundlich model (R^2 = 0.94), confirms its suitability for heterogeneous, multilayer processes, with a KF value of 16.99 mg/g and a heterogeneity factor n = 1.97. Additionally, the pseudo-second-order kinetics model (R^2 = 0.99) indicates rapid interaction between lead ions and the nanoparticles' active sites, achieving a removal efficiency of 91.40% in just 5 minutes of contact. From a thermodynamic perspective, the process is spontaneous and favored at moderate temperatures, with a ΔG^o of -5.89 kJ/mol at 25 °C, although efficiency decreases at higher temperatures. This suggests the need to optimize operating conditions to maximize nanoparticle stability. Furthermore, tests on contaminated water from mining environments confirmed its feasibility under real conditions, reaching adsorption efficiencies above 90% within the first minutes. The green synthesis approach employed in the production of NP-FeO-CL not only provides an efficient material for heavy metal removal but also contributes to the

valorization of agro-industrial waste, promoting circular economy principles and reducing environmental impact. Overall, these findings highlight the great potential of NP-FeO-CL as an accessible and eco-friendly alternative for the purification of heavy metal-contaminated water.

Use of AI tools declaration

The authors declare they have not used Artificial Intelligence (AI) tools in the creation of this article.

Acknowledgments

We would like to thank you for following the instructions above very closely in advance. It will definitely save us lot of time and expedite the process of your paper's publication.

Conflict of interest

All authors declare no conflicts of interest in this paper.

References

1. Hou L, Xing B, Guo H, et al. (2023) Effect of mineralogical characteristics evolution of vermiculite upon thermal and chemical expansions on its adsorption behavior for aqueous Pb (II) removal. *Powder Technol* 430: 119040. https://doi.org/10.1016/j.powtec.2023.119040
2. Ramos D C (2018) Adsorción de cadmio, cobre y plomo en bentonita, caolín y zeolita naturales y modificadas: una revisión de los parámetros de operación, isotermas y cinética. *Ingeniería* 23: 252–273. https://doi.org/10.14483/23448393.13418
3. Sun X, Tang Z, Zheng G, et al. (2024) Effects of different cellular and subcellular characteristics on the atmospheric Pb uptake, distribution and morphology in Tillandsia usneoides leaves. *Plant Physiology and Biochemistry* 207: 108400. https://doi.org/10.1016/j.plaphy.2024.108400
4. De los Santos C R, Barajas F, Pérez H, et al. (2019) Adsorption of copper (II) and cadmium (II) in aqueous suspensions of biogenic nanostructured CaCO 3. *Boletin de la Sociedad Espanola de Ceramica y Vidrio* 58: 2–13. https://doi.org/10.1016/j.bsecv.2018.05.003
5. De la Cueva F, Naranjo A, Puga Torres B, et al. (2021) Presence of heavy metals in raw bovine milk from Machachi, Ecuador. *Granja* 33: 21–30. https://doi.org/10.17163/lgr.n33.2021.02
6. Qian S, Qiongyao Y, Bailin R E N (2025) Adsorption/desorption characteristics of Cd, Cu and Pb on/from soil aggregate fractions from a calcareous soil profile in single and ternary systems. *Pedosphere* 35: 516–525. https://doi.org/10.1016/j.pedsph.2024.02.004
7. Moreno-Perez B, Matamoros-Veloza Z, Rendon-Angeles J C, et al. (2020) Synthesis of silicon-substituted hydroxyapatite using hydrothermal process. *Boletin de la Sociedad Espanola de Ceramica y Vidrio* 59: 50–64. https://doi.org/10.1016/j.bsecv.2019.07.001
8. Deepa K, Prasad C, Jyothi N V V, et al. (2018) Adsorptive removal of Pb (II) metal from aqueous medium using biogenically synthesized and magnetically recoverable core-shell structured AM@ Cu/Fe3O4 nano composite. *Desalination Water Treat* 111: 278–285. https://doi.org/10.5004/dwt.2018.22200

9. Calderón-Tapia C, Medina-Barrera E, Chuquin-Vasco N, et al. (2024) Exploration of bacterial strains with bioremediation potential for mercury and cyanide from mine tailings in 'San Carlos de las Minas, Ecuador. *AIMS Environ Sci* 11: 381–400. https://doi.org/10.3934/environsci.2024019
10. Gómez Aguilar D L, Esteban Muñoz J A, Baracaldo Guzmán D (2020) Tecnologías no convencionales para la remoción de plomo presente en aguas residuales: una revisión bibliográfica 2010-2019. *Tecnura* 24: 97–116. https://doi.org/10.14483/22487638.15849
11. M. de Lourdes Chávez García, A. R. González, A. R. Mejía, et al. Teaching experimental proposal for the synthesis of magnetic nanomaterials. Magnetic nanoparticles in montmorillonite. *Educacion Quimica* 35: 27–42. https://doi.org/10.22201/fq.18708404e.2024.1.85753
12. Srivastava A, Dutta S, Jain R (2023) Waste mediated synthesis of iron nanoparticles using Aegle marmelos peel extract for catalytic degradation of toxic dye contaminants. *RSC Sustainability* 1: 2261–2269. https://doi.org/10.1039/D3SU00246B
13. De la Cueva F, Naranjo A, Puga Torres B, et al. (2021) Presence of heavy metals in raw bovine milk from Machachi, Ecuador. *Granja* 33: 21–30. https://doi.org/10.17163/lgr.n33.2021.02
14. Chávez García M L, Rodríguez González A, Ramos Mejía A, et al. (2024) Teaching experimental proposal for the synthesis of magnetic nanomaterials. Magnetic nano-particles in montmorillonite. *Educacion Quimica* 35: 27–42. https://doi.org/10.22201/fq.18708404e.2024.1.85753
15. Sánchez-Moreno H, García-Rodríguez L, Recalde-Moreno C (2025) Natural cellulose fibers (Agave Americana L. ASPARAGACEAE) impregnated with magnetite nanoparticles as a novel adsorbent of mercury (Hg) in aqueous solutions. *Adsorption* 31: 1-22. https://doi.org/10.1007/s10450-024-00577-1
16. Castillo-Granada A L, Ríos-Calderón O S, Soto-Páez R, et al. (2021) Cómics para el aprendizaje de la espectroscopia infrarroja. *Educación Química* 32: 11-20. https://doi.org/10.22201/fq.18708404e.2021.2.76493
17. Valenzuela-Amaro H M, Vázquez-Ortega P G, Zazueta-Alvarez D E, et al. (2022) Síntesis verde de nanopartículas de magnetita (NPs-Fe3O4): factores y limitaciones. *Mundo Nano. Revista Interdisciplinaria en Nanociencias y Nanotecnología* 16: 1e–18e. https://doi.org/10.22201/ceiich.24485691e.2023.30.69744
18. Tan H L, Lim Y C, Ng L Y, et al. (2023) Plant-mediated synthesis of iron nanoparticles for environmental application: Mini review. *Materials Today: Proceedings* 87: 64-69. https://doi.org/10.1016/j.matpr.2023.02.101
19. Rodríguez A, Fernández L, de Posada J D, et al. (2021) Elucidación de la fórmula estequiométrica de nanohidrotalcitas de mg y ni sintetizadas por el método de coprecipitación. *infoANALÍTICA* 9: 111-134. https://doi.org/10.26807/ia.v9i2.212
20. Sánchez-Moreno H, García-Rodríguez L, Recalde-Moreno C (2025) Natural cellulose fibers from Agave Americana L. ASPARAGACEAE as an effective adsorbent for mercury in aqueous solutions. *Adsorption* 31: 40. https://doi.org/10.1007/s10450-024-00590-4
21. Xia H, Zhang Y, Chen Q, et al. (2023) Unraveling adsorption characteristics and removal mechanism of novel Zn/Fe-bimetal-loaded and starch-coated corn cobs biochar for Pb (II) and Cd (II) in wastewater. *J Mol Liq* 391: 123375. https://doi.org/10.1016/j.molliq.2023.123375

22. Rojas-Bracho L, Farías-Serra P, Santos-Burgoa C, et al. (2023) Epidemia de intoxicación por plomo: su atención desde las normas oficiales mexicanas para proteger la salud de la población. 2023, *Instituto Nacional de Salud Publica* 65: 543-546. https://doi.org/10.21149/15269
23. Naranjo-Jiménez C, WingChing-Jones R (2023) Arsenic, cadmium, mercury, and lead in imported pet food in Costa Rica. *Agronomia Mesoamericana* 34.
24. Calderón H I B, Hernández-Cárabes P, Padilla-Sánchez A J, et al. (2022) Intoxicación por plomo y su impacto en la práctica clínica: artículo de revision. *Ciencia Latina Revista Científica Multidisciplinar* 6: 4176-4189. https://doi.org/10.37811/cl_rcm.v6i1.1792
25. Xu W, Yang T, Liu S, et al. (2022) Insights into the Synthesis, types and application of iron Nanoparticles: The overlooked significance of environmental effects. *Environment International* 158: 106980. *https://doi.org/10.1016/j.envint.2021.106980*
26. Ramos D C (2018) Adsorción de cadmio, cobre y plomo en bentonita, caolín y zeolita naturales y modificadas: una revisión de los parámetros de operación, isotermas y cinética. *Ingeniería* 23: 252-273. https://doi.org/10.14483/23448393.13418
27. Kalam S, Abu-Khamsin S A, Kamal M S, et al. (2021) Surfactant adsorption isotherms: A review. *American Chemical Society* 6: 32342-32348. https://doi.org/10.1021/acsomega.1c04661
28. Al-Dhawi B, Kutty S, Alawag A, et al. (2024) Lithium recovery in a batch adsorption study: Synthesis, characterization, optimization, regeneration, kinetics, and isotherm studies. *Sci Afr Sci Afr* 26: e02449. *https://doi.org/10.1016/j.sciaf.2024.e02449*
29. de Lourdes Colín-Álvarez M, Calderón-Domínguez G, Rojas-Candelas L E, et al. Aplicación de la nanotecnología como innovación en recubrimientos alimentarios. *Pädi Boletín Científico de Ciencias Básicas e Ingenierías del ICBI* 12: 21–33. https://doi.org/10.29057/icbi.v12iEspecial.12127
30. Ciobanu C S, Iconaru S L, Le Coustumer P, et al. (2012) Antibacterial activity of silver-doped hydroxyapatite nanoparticles against gram-positive and gram-negative bacteria. *Nanoscale Res Lett* 7. https://doi.org/10.1186/1556-276X-7-324
31. Maleki S, Abedi E, Hashemi S M B (2024) Insights into kinetic, isotherm, and thermodynamic of ultrasound mode-and amplitude-dependent carotenoid and chlorophyll degradation or/and adsorption. *Ultrason Sonochem* 111: 107130. https://doi.org/10.1016/j.ultsonch.2024.107130
32. Chu K H, Hashim M A, Basirun A A (2025) Removal of antibiotic contaminants from water via adsorption: Analysis of equilibrium isotherms. *Environmental Pollution and Management* https://doi.org/10.1016/j.epm.2025.06.001
33. Tran H N (2023) Applying linear forms of pseudo-second-order kinetic model for feasibly identifying errors in the initial periods of time-dependent adsorption datasets. *Water (Switzerland)* 15: 1231. https://doi.org/10.3390/w15061231
34. Liu Y, Chen Y, Li Y, et al. (2024) Immobilization of Pb in waste water and soil by tourmaline-biochar composites (TBs): Characteristics and mechanisms. *Science of the Total Environment* 920: 170803. https://doi.org/10.1016/j.scitotenv.2024.170803
35. Martini S, Afroze S, Roni K A, et al. (2021) A review of fruit waste-derived sorbents for dyes and metals removal from contaminated water and wastewater. *Desalination Water Treat* 235: 300–323. https://doi.org/10.5004/dwt.2021.27658

36. Pascua M J, Romero M L (2020) Remoción de plomo en solución acuosa usando criogeles basados en polyacrylamide como adsorbente: Estudio de equilibrio en modo batch. *Revista Torreón Universitario* 9: 77–93. https://doi.org/10.5377/torreon.v9i25.9855
37. Morsa A, Yazhenskikh E, Ziegner M, et al. (2025) Experimental study and thermodynamic assessment of the MgSO4-CaSO4 system. *Calphad* 90: 102855. https://doi.org/10.1016/j.calphad.2025.102855
38. Hakim L, Widiarman M (2024) Adsorbent performance of nipa (nypafruticans) frond in methylene blue dye degradation: Response surface methodology optimization. *AIMS Environ Sci* 11: 38–56. https://doi.org/10.3934/environsci.2024003
39. Elles-Pérez C J, Muñoz-Acevedo A, Guzmán A, et al. (2025) Optimized diclofenac sodium adsorption on Lecythis minor-derived activated carbon: Kinetics and isotherm analysis. *J Mol Liq* 2025: 127987. https://doi.org/10.1016/j.molliq.2025.127987
40. Lavado-Meza C, Sun-Kou M R, Castro-Arroyo T K, et al. (2020) Biosorción de plomo (II) en solución acuosa con biomasa de los cladodios de la tuna (opuntia ficus indica). *Revista Colombiana de Quimica* 49: 36–46. https://doi.org/10.15446/rcq.v49n3.85823
41. Siraj K, Aballa J S, Danish M, et al. (2024) The effect of microwave and muffle furnace-assisted heating on the surface characteristics of teff husk activated carbons: Thermodynamic, isotherm, and kinetics study of Pb removal. *Diam Relat Mater* 143: 110912. https://doi.org/10.1016/j.diamond.2024.110912
42. Trong N T, Le Tan P H, Ngoc D N, et al. (2024) Optimizing the synthesis conditions of aerogels based on cellulose fiber extracted from rambutan peel using response surface methodology. *AIMS Environ Sci* 11: 576–592. https://doi.org/10.3934/environsci.2024028
43. Marcelo R V (2022) Kinetics and Adsorption Mechanisms of Lead (II) Using Gis-NaP Zeolite Obtained from Brick Waste. *Revista Politecnica* 50: 63–70. https://doi.org/10.33333/rp.vol50n2.07
44. Rodrigues D S, Alves L F, Meyer J F C A, et al. (2025) IN VITRO POPULATION GROWTH OF HUMAN GLIOBLASTOMAS: REAL PATIENTS AND CURVE FITTING. *Hematol Transfus Cell Ther* 47: 103807. https://doi.org/10.1016/j.htct.2025.103807
45. De los Santos C R, Barajas F, Pérez H, et al. (2019) Adsorption of copper (II) and cadmium (II) in aqueous suspensions of biogenic nanostructured CaCO 3. *Boletin de la Sociedad Espanola de Ceramica y Vidrio* 58: 2–13. https://doi.org/10.1016/j.bsecv.2018.05.003

AIMS Press